Implantable MIMO Antenna Design for High Data Rate Wireless Capsule Endoscopy

LIU, CHANG

How to cite:

LIU, CHANG (2026). *Implantable MIMO Antenna Design for High Data Rate Wireless Capsule Endoscopy*, Durham e-Theses. http://etheses.dur.ac.uk/16470/

Implantable MIMO Antenna Design for High Data Rate Wireless Capsule Endoscopy

Liu Chang

A Thesis presented for the degree of
Doctor of Philosophy

Department of Engineering
Durham University
United Kingdom
June 2019

Abstract

Antenna performance is strongly constrained by physical size, which becomes a major challenge in wireless capsule endoscopy (WCE) due to the extremely limited internal space. In addition to compactness and wide bandwidth, practical WCE telemetry must remain reliable under strong in-body attenuation, detuning, and random capsule orientation. To address these constraints and to enable higher-throughput links for high-resolution imaging, this work proposes a multistage antenna design strategy for WCE, covering conformal, miniaturised, and transparent antenna structures.

In Stage I, a conformal antenna is developed based on a left–right symmetric tri-arm dipole printed on a flexible substrate and deployed along the capsule inner cylindrical wall. Multiple resonant modes are introduced and optimised to improve impedance matching and to realise ultra-wideband (UWB) operation. The final design occupies $30.5\,\mathrm{mm} \times 9\,\mathrm{mm} \times 0.04\,\mathrm{mm}$ and achieves a -10 dB impedance bandwidth of 0.59–1.36 GHz (fractional bandwidth 78.97%).

Stage II introduces dielectric hollowing to reduce the effective permittivity while maintaining the external capsule geometry, enabling the integration of a dual-element multiple-input multiple-output (MIMO) system. Each element occupies only $7.192\,\mathrm{mm}^3$ and operates from 0.61 to 1.51 GHz (fractional bandwidth 84.91%), with low envelope correlation (ECC < 0.1) and good isolation ($>$ 20dB). The MIMO configuration is adopted to improve link robustness and channel capacity under orientation uncertainty and multipath scattering in the gastrointestinal tract, supporting a target telemetry data rate of $10 - 120$ Mb/s for high-resolution capsule imaging.

In Stage III, a transparent antenna is developed to share the limited frontal area with the capsule camera. A conductivity–frequency model is established for inkjet-printed silver mesh conductors with 50–90% optical transparency over 0–6 GHz. Based on this model, a circularly polarised coplanar waveguide (CPW) fed circular patch antenna is designed, operating from 2–3 GHz with 70% measured optical transparency.

All antennas are simulated using Ansys HFSS and CST Studio Suite, fabricated using appropriate materials, and evaluated using pork tissue under controlled laboratory conditions to approximate in-body propagation. The measured results validate the proposed multistage framework, demonstrating wideband operation, strong miniaturisation with MIMO capability, and optically transparent integration for camera-constrained WCE platforms.

Declaration

The work in this thesis is based on research carried out at the Department of Engineering, Durham University, United Kingdom. No part of this thesis has been submitted elsewhere for any other degree or qualification and it is all my own work unless referenced to the contrary in the text.

Acknowledgements

I would like to express my sincere gratitude to my supervisors, Dr Ismail Ben Mabrouk and Dr Ikhlef Aissa, for their continuous guidance, encouragement, and invaluable academic support throughout the course of this research. Their expertise and constructive feedback have been instrumental in shaping both the technical depth and overall direction of this thesis.

I would also like to thank Dr Simorangkir, Roy B.V. for his collaboration and insightful discussions, which greatly contributed to the development of several aspects of this work. In addition, I am grateful to Professor Andrew Gallant, a member of my review team, for his thoughtful comments and valuable suggestions, which helped improve the quality and clarity of this thesis.

Special thanks are extended to the staff of the Electronic Workshop, particularly Neil and Dave, for their technical assistance in antenna fabrication, assembly, and soldering. Their practical support was essential to the successful realization of the experimental prototypes presented in this thesis.

Finally, I would like to thank my family and friends for their constant support, patience, and encouragement throughout my doctoral studies. Their understanding and motivation have been invaluable during this journey.

Contents

List of Figures

List of Tables

Dedication

To my family.

CHAPTER 1

Introduction

1.1 Research Background

Wireless communication represents a significant milestone in human technological development, fundamentally transforming modes of production and social interaction. In 1864, physicist James Clerk Maxwell formulated the mathematical framework unifying electric and magnetic fields, laying the theoretical foundation for electromagnetic wave propagation. In 1888, Heinrich Hertz experimentally validated the existence of electromagnetic waves through spark-gap experiments, providing the first direct evidence for Maxwell's theory. In 1901, Guglielmo Marconi successfully received the first transatlantic wireless signal in Newfoundland, transmitted from England, marking the transition of wireless communication from theoretical speculation to practical realization.

As devices for transmitting and receiving electromagnetic waves, antennas are essential components of wireless communication systems. The receiving apparatus employed in the experiments of Hertz and Marconi can be regarded as early prototypes of modern antennas. Functionally, antennas convert electrical signals propagating in conductors into electromagnetic waves capable of traveling through space, and vice versa. By enabling the transformation of information carriers from electrons to electromagnetic waves, antennas serve as a bridge between wired and wireless communication, and as a key link between circuit theory and electromagnetic field theory.

In the 21st century, the rapid expansion of application scenarios has driven significant advances in wireless-enabled medical devices. These systems, ranging from wearable health monitors to implantable diagnostic tools, impose unique constraints on antenna design due to strict size limitations, biocompatibility requirements, and operation in lossy biological media. Among these, wireless capsule endoscopy (WCE) has emerged as a transformative technology for gastrointestinal diagnostics.

1.1.1 Operation of WCE

Over the past two decades, gastrointestinal diseases have become increasingly prevalent. According to [6], the incidence rate of gastrointestinal cancers has risen from approximately 2,000–2,500 cases per 100,000 people to around 4,000 cases in recent years, highlighting the growing demand for reliable diagnostic techniques for the digestive tract, as shown in Fig. 1.1.

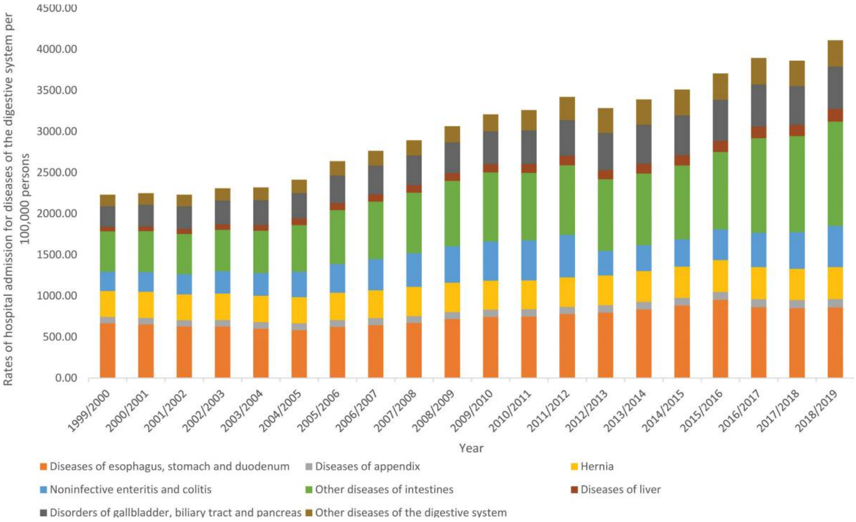

Figure 1.1: Hospital admission rates due to DDS in England and Wales stratified by type between 1999 and 2019. DDS = diseases of the digestive system [1].

Conventional wired endoscopy, while effective, is invasive, requires sedation, and offers limited patient comfort. In contrast, WCE eliminates the need for physical insertion, causes no pain, does not require sedation, and can operate inside the body for a long period. The operation of WCE follows a simple but well-coordinated process, as shown in Fig. 1.2. After the patient swallows the capsule, it moves through the gastrointestinal tract by natural muscle movement. The capsule can stay in the body long enough to capture continuous images during the entire journey. During this time, the built-in imaging module takes clear pictures of the digestive tract lining, while the antenna sends the data wirelessly to a receiver worn by the patient. The data are then sent to a cloud server or hospital computer for storage and analysis. After the examination, the capsule leaves the body naturally without any medical procedure. Doctors then review the images to make a diagnosis. This process reduces patient discomfort and enables a full examination of the digestive tract.

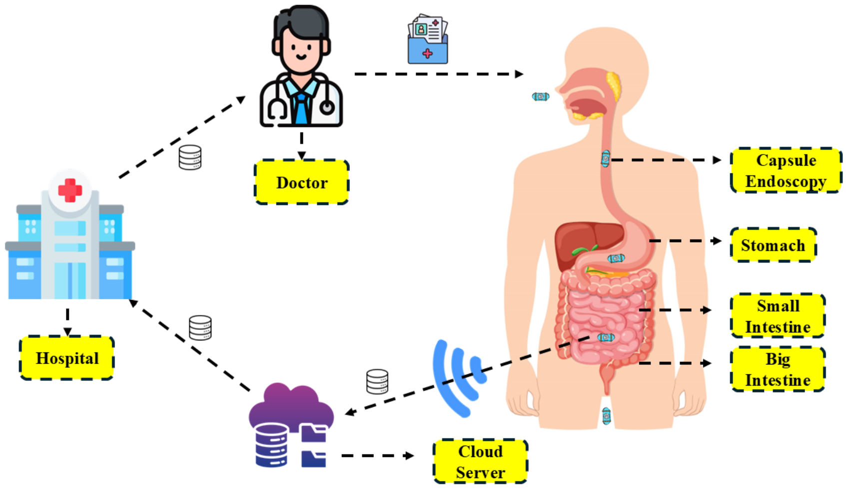

Figure 1.2: Schematic diagram of wireless monitoring system based on WCE

1.1.2 Development of WCE

First introduced in 2000 by Israeli engineer Gavriel Iddan and gastroenterologist Eitan Scapa [1], the initial WCE prototype measured only 11 × 23 mm, small enough to be swallowed without discomfort. It integrated a short-focal-length optical system, a CMOS image sensor, white-light LED illumination, and an application-specific integrated circuit (ASIC) transmitter operating in the UHF band. The system was capable of capturing high-quality images of the gastrointestinal tract without air insufflation and transmitting them wirelessly to an external receiver for more than five hours, with continuous video transmission lasting up to six hours during trials. In the first human studies involving ten healthy volunteers, the capsule successfully imaged the stomach, small bowel, and terminal ileum, and was naturally excreted without complications, demonstrating the feasibility of untethered gastrointestinal imaging. While these early results demonstrated the feasibility of wireless endoscopy, they also revealed critical challenges in antenna design. The extremely limited internal volume of the capsule restricted antenna size, leading to reduced bandwidth, low gain, and frequency detuning in the in-body environment. These issues degraded image transmission quality and reliability, ultimately affecting diagnostic performance. As a result, subsequent research has focused on developing compact antennas with improved bandwidth and radiation efficiency to meet the stringent communication requirements of WCE applications. Several representative strategies for antenna miniaturization can be summarized as follows:

- Geometrical modifications – Early methods focused on folding or winding metallic conductors into compact shapes such as helical or cylindrical structures, reducing the physical size of the antenna while preserving resonance.

- High-permittivity substrates – The introduction of artificial dielectric materials with high permittivity enabled further miniaturization by shortening the effective wavelength, thereby reducing the required antenna dimensions.

- Conformal and flexible designs – More recent approaches employ conformal structures built on flexible dielectric substrates, allowing antennas to adapt to curved surfaces while achieving sufficient electrical length with minimal occupied volume.

These miniaturization strategies laid the technological foundation for antenna design in emerging biomedical applications. In particular, wireless capsule endoscopy (WCE) imposes far more stringent requirements due to its extreme volume constraints, lossy in-body propagation environment, and the need for reliable high-data-rate communication. As a result, the three major approaches—geometrical modification, high-permittivity substrates, and conformal flexible designs—have been extensively adapted and further refined for WCE antenna development. The following section provides a detailed review of how these strategies have evolved within the context of WCE, highlighting key design trends, representative structures, and their corresponding advantages and limitations.

1.1.3 Thesis Structure

This research is centered on the concept of multi-resonance, approached from the perspective of antenna design. It explores and summarizes the underlying theory of multi-resonant structures, and on this basis proposes several high-performance miniaturized antenna designs. The overall structure of the thesis is illustrated in Fig. 1.3.

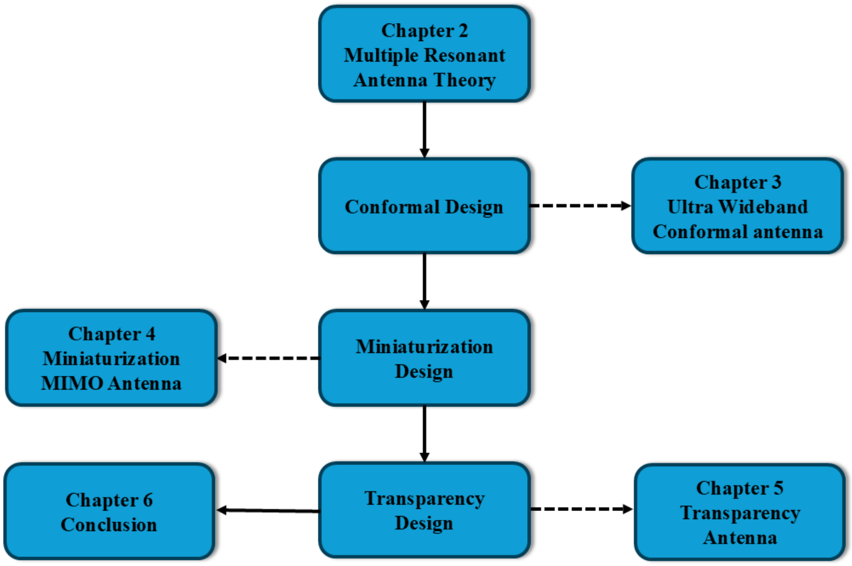

Figure 1.3: Paper structure diagram

Chapter 2 establishes the theoretical foundation of this research, providing a systematic summary of multi-resonance from the perspective of antenna design. The chapter begins with the fundamental theory of multi-resonance, extends to the analysis of resonance modes, and discusses the underlying working principles of antennas. It further examines the impact of application environments on design strategies, thereby forming a theoretical framework for miniaturized antenna design tailored to WCE. Finally, the chapter reviews existing research and design solutions to validate the practical feasibility of the proposed theories.

Chapter 3 focuses on conformal antenna design. It begins with a review and analysis of existing conformal antennas developed for WCE applications, highlighting their structural configurations and design characteristics. Building upon these insights, the chapter introduces a novel conformal antenna based on a dipole structure combined with multi-resonance techniques, which achieves ultra-wideband performance to meet the stringent communication requirements of WCE systems.

Chapter 4 addresses antenna miniaturization and the integration of multiple-input multiple-output (MIMO) techniques in WCE systems. The chapter first discusses the challenges posed by the extremely limited capsule volume, particularly for multi-antenna integration, where further size reduction must be balanced against increased coupling between antenna elements. To overcome these limitations, a dielectric hollowing strategy is proposed, which reduces the effective antenna volume without altering the overall capsule dimensions. Based on this method, a dual-element MIMO antenna system is developed and evaluated in terms of impedance characteristics, bandwidth, isolation, envelope correlation coefficient (ECC), and channel capacity. The results demonstrate that the proposed design significantly improves spatial efficiency while supporting reliable high-data-rate communication.

Chapter 5 investigates the use of transparent antennas in WCE systems. With the limited internal volume of the capsule restricting the number of antennas, transparent designs offer the possibility of utilizing the space in front of the camera without obstructing imaging quality. To enable this, transmission lines were first fabricated using inkjet-printing technology, and a mapping between optical transparency and electrical conductivity was established. Guided by this relationship, a transparent patch antenna was designed, achieving the required operating band while maintaining high optical transmittance. This approach provides a novel solution for increasing antenna integration in WCE while preserving both imaging performance and aesthetic appearance.

Chapter 6 summarizes the work presented in this thesis and outlines possible directions for future research.

CHAPTER 2

The Design of Conformal Antenna with UWB Characteristic

2.1 Literature Review

WCE is capable of capturing numerous high-definition pictures and videos in the Gastrointestinal Tract. To ensure rapid and stable data transmission from these devices to medical institutions or cloud servers, antennas with wide bandwidths are crucial for facilitating reliable and efficient high-data-rate transmission [7].

In addition, the antenna with wideband characteristic is an effective solution for addressing the detuning issue. The human body is a complex biological system comprising various tissues and fluids. It exhibits diverse electromagnetic properties that can influence medical antenna resonant frequencies and radiation pattern. This phenomenon is referred to as frequency detuning. Furthermore, the body's movements and postures can modify the antenna's operational environment, altering its performance parameters. In order to address this challenge, the ultra-wide bandwidth antenna will be designed. Therefore, researchers have actively explored novel antenna design methods to fulfill wideband frequency within limited space constraints. Das and Yoo design a conformal antenna with open slots to increase the bandwidth with 26mm × 11mm capsule dimensions. Utilizing Rogers ULTRALAM 3850HT as the substrate, they achieved an impedance bandwidth of 20.21% and an antenna volume of 107mm^3 (53.5mm × 10mm × 0.2mm) [8]. In 2018, Ke et al. [9] minimized the antenna size by incorporating T-slots to extend the current path of the antenna and utilized a flexible polyimide substrate. Polyetheretherketones (PEEK) material was employed for the capsule shell with dimensions of 22mm × 11mm, resulting in a fractional bandwidth of 8.85%. Kuo and Ruipeng studied a double spiral arms structure to increase the current path and minimize the antenna , utilizing polyimide as the substrate [10]. The antenna, enclosed within a hemispherical capsule of dimensions $\pi \times 3^2 \times 26$ mm^3, demonstrated an enhanced bandwidth of 39.16% at the lower band and 12.06% at the higher band. Duan and Xu proposed a design concept to design a circularly polarized omnidirectional radiation antenna, consisting of two rotatable antennas, realized circular polarization in the entire azimuth plane, and utilized FR4 substrate [11]. Their antenna exhibited a bandwidth of 18.58%, and its volume measured at 2090.73mm^3 ($\pi \times 5.5^2$mm × 22mm), enclosed within a shell of dimensions 11mm × 22mm. Lei et al. and Ketavath et al. investigated a dual-polarized conformal antenna for implantable medical devices (IMDs) in their respective studies [12, 13]. Lei et al.'s design, encapsulated within a 26mm × 11mm capsule, had dimensions of 15mm × 15mm × 1.27mm and exhibited a bandwidth of 67.5%. Conversely, Ketavath et al.'s design was slightly larger, measuring 22mm × 24mm × 0.07mm, and achieved a fractional bandwidth of 15.3%.

Although previous studies have demonstrated the effectiveness of conformal and wideband design strategies, none of the reported antennas simultaneously achieve compact integration within a capsule and an ultra-wide fractional bandwidth. Most conformal structures offer only moderate bandwidths (typically below 40%), while designs with higher bandwidths often require larger volumes that exceed the size constraints of commercial WCE capsules. In addition, several polarization-diverse or spiral-based configurations improve impedance matching, but still fail to provide sufficient bandwidth for high-data-rate video transmission. These limitations highlight a critical research gap: the lack of an antenna that combines compact conformal geometry with UWB suitable for WCE. This gap motivates the present work, which investigates a flexible conformal antenna capable of providing wideband performance under the stringent spatial and electromagnetic constraints of capsule endoscopy.

2.1.1 Development of Antenna Miniaturization Techniques

Early studies on antenna miniaturization primarily pursued direct reductions in physical size while maintaining acceptable performance. Because many of these designs were tailored to specific systems, they offered limited general principles. This motivated investigations into the theoretical limits of how small an antenna can be made and still perform adequately. With these fundamental constraints in mind, practical design practice treats miniaturization as a multi-objective trade-off among efficiency, bandwidth, size, and radiation characteristics. A representative example of subsequent development is the wideband thick-arm spiral antenna reported by Sang Heun Lee and colleagues [2]. The antenna occupied only 10 mm in diameter and 5 mm in height, yet achieved about 21% fractional bandwidth centered at 500 MHz (446–550 MHz, VSWR < 2) with an isotropic radiation pattern suitable for unpredictable capsule orientations, as Fig 2.1. Its performance was validated in both a liquid human phantom ($\varepsilon_r \approx 56.9$, $\sigma \approx 0.97$ S/m) and a live pig under general anesthesia, showing received power levels around -60 dBm for a 0 dBm transmit,

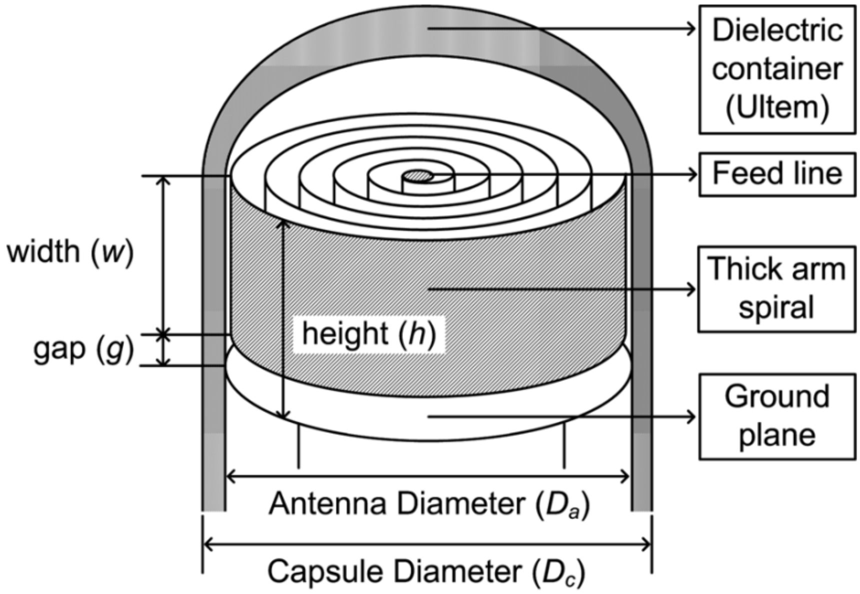

Figure 2.1: Geometry of the designed thick-arm spiral antenna with the capsule [2].

which satisfied biotelemetry sensitivity requirements. When integrated into a complete capsule system with a CMOS imager, LEDs, and an OOK transceiver, the antenna enabled real-time wireless image transmission at 340 × 340 pixels and 10.5 fps with a data rate of 20 Mb/s, confirming its suitability for wideband capsule endoscopy applications.

While geometrical modifications such as spiral structures can effectively reduce antenna size and improve bandwidth, further miniaturization often requires alternative approaches. One widely explored method is the use of high-permittivity substrates, which shorten the guided wavelength and allow the antenna dimensions to be reduced without compromising resonance. A representative study in this direction is the multilayer circularly polarized (CP) helical antenna proposed by Liu [3]. The antenna was implemented on Rogers RO3010 substrates with a dielectric constant of 10.2 and a thickness of 25 mil, forming a compact three-layer axial-mode helical structure interconnected by vias, as Fig 2.2. With a radius of 5.5

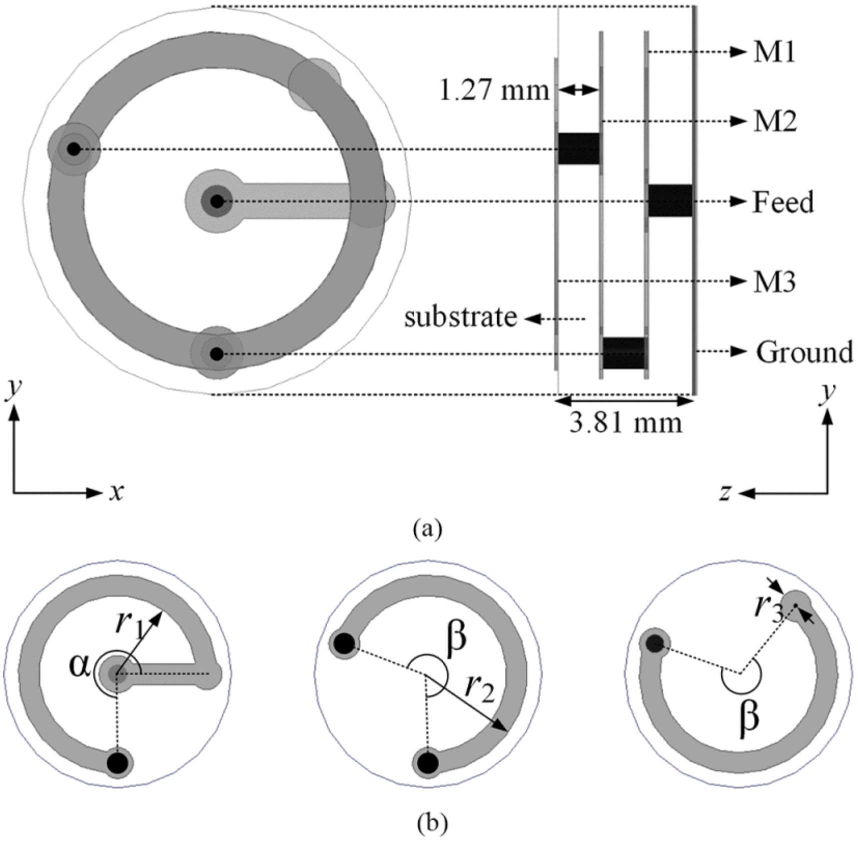

Figure 2.2: Configuration of the helical antenna. (a) top view and side of the proposed antenna. (b) top view of three metal layers [3].

mm and a height well within typical capsule limits, the antenna achieved a measured impedance bandwidth of about 26% and an axial ratio bandwidth of 33% across the 2.4–2.48 GHz ISM band. Its performance was validated through simulations, in-vitro measurements using a muscle phantom, and evaluations in a voxel-based human body model, demonstrating stable impedance matching and circular polarization at different implant positions including the stomach, small intestine, and colon. Furthermore, the study considered the effect of biocompatible coatings such as PEEK (0.05 mm) and showed that frequency shifts induced by packaging could be compensated through design optimization. Overall, this work confirmed that high-permittivity substrates provide an effective route for miniaturizing WCE antennas while maintaining adequate bandwidth and polarization purity, thereby supporting high-data-rate capsule endoscopy applications.

While high-permittivity substrates can reduce antenna dimensions, they often introduce narrower bandwidths and efficiency losses. An alternative approach is to employ conformal designs on flexible substrates, allowing the antenna to utilize the capsule's outer wall while achieving sufficient electrical length and saving internal volume.

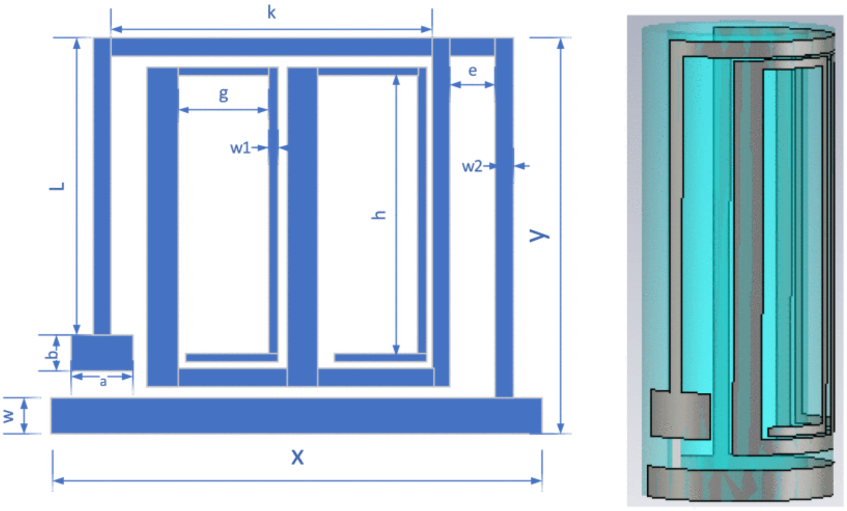

(a) (b)

Figure 2.3: (a) Geometric design of proposed antenna. (b) Physical layout model of designed antenna on the surface of capsule. [4].

A notable example is the conformal ultra-wideband antenna reported in [4]. The design used a meander-line structure printed on Rogers 5870 substrate ($\varepsilon_r =$

2.55, thickness 0.79 mm), which was then bent around the outer surface of a capsule with a 3 mm radius. The conformal antenna occupied an area of 15 × 15 mm^2 and operated robustly within the capsule's cylindrical geometry, as Fig 2.3. Simulations and measurements in tissue-equivalent liquids ($\varepsilon_r \approx 56$, $\sigma \approx 0.8$ S/m) confirmed an ultrawide bandwidth of 284–825 MHz ($\approx$ 541 MHz, $S_{11} < -10$ dB), covering both the MedRadio (401–406 MHz) and 433–434 MHz ISM bands. The antenna maintained an omnidirectional radiation pattern, with a maximum realized gain of -31.5 dBi at 403 MHz, and satisfied SAR compliance with an input power below 1.7 mW. Moreover, the study analyzed the impact of bending radius, capsule shell thickness, and internal batteries, showing only minor influence on impedance matching and radiation characteristics. This demonstrated that conformal flexible designs not only provide wide bandwidth and robustness against detuning in different tissue environments, but also relax fabrication tolerances, making them practical for large-scale WCE applications.

Overall, in the development of WCE antennas, the demand for miniaturization has remained constant, aiming to maximize the utilization of the limited capsule volume. At the same time, increasing requirements have been imposed on communication performance, including higher spectral efficiency, broader frequency coverage, and reduced losses from lumped components. Meeting these requirements involves additional technical challenges, such as multiple-input multiple-output (MIMO) antenna integration, inter-element decoupling, and the design of efficient matching networks and feeding structures. Conventional design approaches offer limited freedom for further improvement under these constraints. To address these challenges, this thesis proposes a new antenna design methodology that leverages multi-resonance structures together with conformal, miniaturization, and transparent techniques to maximize spatial efficiency and enhance the overall performance of WCE systems.

2.1.2 Ultra-Wideband Requirement and Current Status

In addition to miniaturization, bandwidth has become a critical design requirement for WCE antennas. High-resolution imaging and real-time video transmission demand high data rates, which cannot be supported by narrowband antennas. Ultra-wideband (UWB) operation provides sufficient channel capacity, enables higher frame rates, and ensures reliable communication even in the presence of frequency detuning caused by lossy biological tissues. Moreover, UWB performance allows the antenna to cover multiple allocated frequency bands, thereby increasing compatibility with different medical telemetry standards.

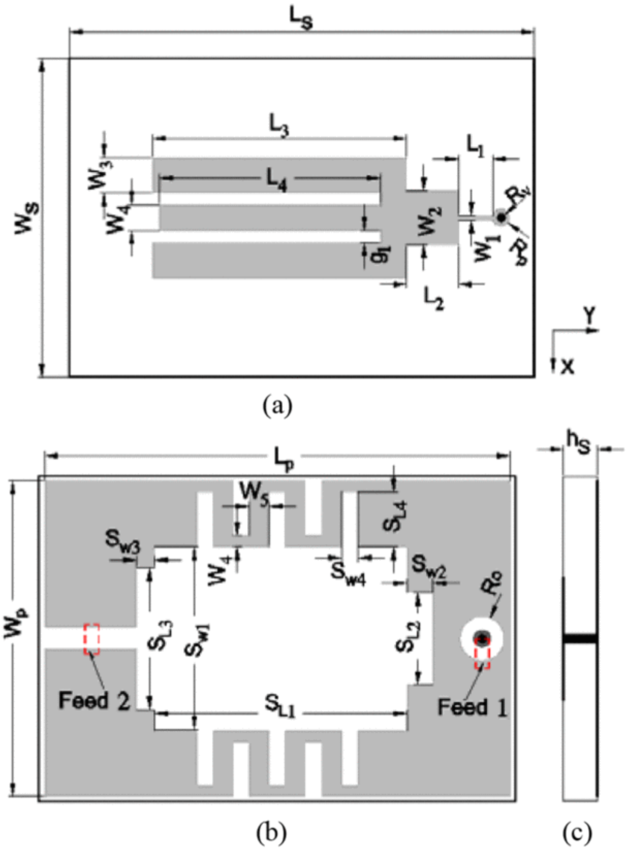

(a)

(b)

(c)

Figure 2.4: Planar structure of the capsule antenna. (a) Top view. (b) Bottom view. (c) Side view. [5].

A representative work on UWB antennas for WCE is the conformal dual-polarized design reported in [5]. The antenna consists of a step-shaped monopole and an irregular rectangular loop printed on opposite sides of a dielectric substrate, which are rolled to conform to the capsule's cylindrical wall. The monopole provides a fundamental wideband response, while the loop introduces additional resonances through current coupling, as Fig 2.4. By combining multiple resonant paths and utilizing conformal geometry, the antenna achieves wide impedance matching from 2 to 14 GHz and provides dual polarization with high port isolation, ensuring reliable operation across multiple medical telemetry bands. Although this design demonstrates excellent bandwidth performance, its underlying principle remains an extension of printed patch-type structures, relying heavily on geometric modifications of planar elements.

At present, most UWB antenna research for WCE has focused on similar patch-based configurations, which, while effective, often involve complex layouts and limited design flexibility. In contrast, this dissertation explores alternative pathways toward UWB performance by leveraging dipole-based structures, including folded dipoles and loop antennas. By introducing multi-resonant mechanisms into these simpler radiating forms and integrating them with conformal geometries, new designs are proposed that achieve ultra-wideband operation while maintaining compactness and suitability for capsule integration.

2.2 Basic Theory

This section approaches antenna design from a theoretical perspective, beginning with the fundamental principles of single-resonance antennas and extending to the concept of multi-resonance. Through representative design examples, the mechanisms of bandwidth enhancement are analyzed, and the theoretical framework of multi-resonant UWB operation for WCE applications is summarized. Finally, three representative antenna types—dipoles, folded dipoles, and loop antennas—are reviewed in terms of their structures and underlying theories, providing the foundation for the detailed designs presented in subsequent chapters.

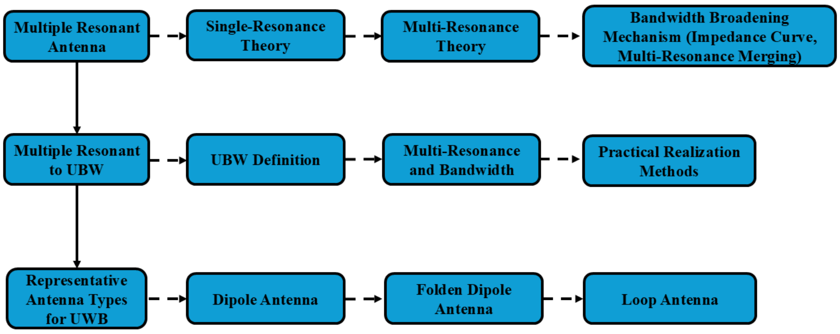

Figure 2.5: Chapter 2 structure diagram

The first part introduces multi-resonance theory, starting from single-resonance antennas and extending to the principles of multi-resonance, followed by an explanation of how multi-point optimization can be used to achieve UWB performance.

The second part examines the relationship between multi-resonance and UWB, including the definition of UWB, its design criteria, and representative theoretical approaches for wideband operation.

The third part focuses on three representative antenna structures—dipole, folded dipole, and loop antennas—analyzing their resonant characteristics and discussing how they may be combined with multi-resonance principles to realize UWB performance.

2.2.1 Single-Resonance Theory

The resonant behavior of an antenna can often be approximated using a lumped RLC circuit model. Depending on the dominant resonance mechanism, a single-resonant antenna may be represented as either a series or a parallel connection of resistance R, inductance L, and capacitance C, as Fig. 2.6.

Both models share the same fundamental resonance condition as (2.1), but they differ in impedance characteristics, quality factor, and bandwidth properties.

$$\omega_0 = \frac{1}{\sqrt{LC}} \tag{2.1}$$

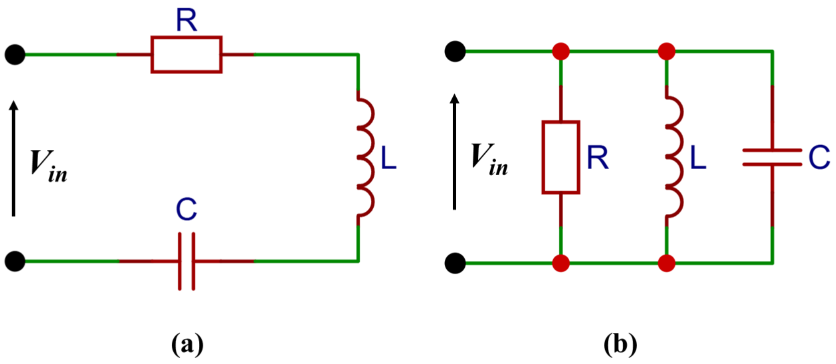

Figure 2.6: Equivalent RLC models for single-resonant antennas: (a) Series RLC, (b) Parallel RLC

For dipole- or monopole-type radiators, where the radiation resistance dominates, the antenna can be modeled by a series RLC circuit (2.2)

$$Z_{\text{series}}(\omega) = R + j\left(\omega L - \frac{1}{\omega C}\right) \tag{2.2}$$

At resonance, the inductive and capacitive reactances cancel out, and the input impedance reduces to a purely real value $Z(\omega_0) = R$. This corresponds to the maximum current condition, which is analogous to the antenna radiating most efficiently at its resonant frequency. The quality factor is expressed as 2.3

$$Q_s = \frac{\omega_0 L}{R} = \frac{1}{\omega_0 RC} \tag{2.3}$$

and the fractional bandwidth(FBW) is approximately as (2.12)

$$\text{FBW} \approx \frac{1}{Q_s} \tag{2.4}$$

For patch- or loop-type resonant structures, which primarily store energy, the antenna is better represented by a parallel RLC circuit as (2.5)

$$Y_{\text{parallel}}(\omega) = \frac{1}{R} + j\left(\omega C - \frac{1}{\omega L}\right) \tag{2.5}$$

At resonance, the reactive components cancel, resulting in a maximum input impedance. The corresponding quality factor is (2.6)

$$Q_p = \frac{R}{\omega_0 L} = \omega_0 RC \tag{2.6}$$

and the bandwidth is again inversely proportional to Q_p. A higher quality factor implies a sharper resonance and narrower bandwidth, while a lower quality factor corresponds to broader bandwidth but reduced efficiency.

From a physical perspective, L is associated with the magnetic energy stored in the current path, C with the electric energy stored in the fringing fields, and R with both radiation and ohmic losses. The quality factor can also be defined more generally as (2.7)

$$Q = \omega_0 \frac{W_e + W_m}{P_{\text{diss}}} \tag{2.7}$$

where W_e and W_m are the stored electric and magnetic energies, and P_{diss} is the total power dissipated through radiation and loss.

In practice, the lossy and dispersive properties of biological tissues strongly influence the effective R, L, and C parameters. Higher permittivity values increase the effective electrical length, shifting the resonant frequency downward, while higher conductivity increases losses, reducing Q and broadening the bandwidth but at the expense of efficiency. These effects explain why WCE antennas must be designed with wideband or ultra-wideband performance, not only to support high data rates but also to maintain reliable operation in the presence of tissue-induced detuning.

In summary, whether represented by a series or parallel RLC circuit, a single-resonant antenna is inherently limited to a narrow bandwidth, with the fractional bandwidth approximately proportional to $1/Q$. To overcome this limitation, additional resonances must be introduced so that their impedance responses overlap in frequency, thereby forming a continuous wideband or even ultra-wideband characteristic. This principle underpins the multi-resonance theory discussed in the following section.

2.2.2 Multiple-Resonance Theory

In practical antenna design, the bandwidth limitation of a single resonance can be overcome by introducing multiple resonances. When two or more resonant frequencies are properly positioned within close proximity, their impedance responses overlap, resulting in a continuous wideband characteristic. This principle is the essence of multiple resonance theory.

The mechanism can be realized in different ways. For example, additional resonances may be generated through structural modifications such as parasitic elements, slots, or stubs, or by exciting higher-order modes that coexist with the fundamental mode. In each case, the key objective is to control the location and coupling of resonant frequencies so that the combined response forms a smooth impedance curve across a broad frequency range.

Multiple resonance thus provides a systematic route toward wideband and even UWB antenna design, serving as the theoretical foundation for many modern configurations.

Multiple resonance can be intuitively explained using the extension of the lumped RLC model. When additional resonant branches are introduced in either a series or a parallel configuration, multiple resonant frequencies appear, and their combined impedance response leads to bandwidth enhancement.

In the case of series resonance, several RLC sections are cascaded along the current path, each contributing its own resonant frequency. The overall input impedance can be expressed as the sum of the impedances of the individual resonant circuits,

$$Z_{\text{total}}(\omega) = \sum_{k=1}^{N} \left(R_k + j\left(\omega L_k - \frac{1}{\omega C_k} \right) \right), \tag{2.8}$$

where each pair (L_k, C_k) defines a resonant frequency $\omega_{0k} = 1/\sqrt{L_k C_k}$. As these resonances are placed in close spectral proximity, their impedance minima overlap, producing a continuous wideband response.

For parallel resonance, multiple branches consisting of RLC circuits are connected across the input port. The input admittance is then given by the sum of the admittances of each branch,

$$Y_{\text{total}}(\omega) = \sum_{k=1}^{N} \left(\frac{1}{R_k} + j \left(\omega C_k - \frac{1}{\omega L_k} \right) \right). \tag{2.9}$$

In this case, each branch generates a high-impedance resonance peak at its natural frequency, and the superposition of these peaks forms a broadened impedance profile.

From a frequency-domain perspective, series coupling produces multiple low-impedance valleys, whereas parallel coupling produces multiple high-impedance peaks. In both cases, the overlap of adjacent resonances effectively stitches together several narrow frequency ranges into a wideband operating region. This principle provides the foundation for many modern wideband and UWB antenna designs.

Another important mechanism for bandwidth enhancement is the excitation and combination of multiple resonant modes within a single antenna structure. For a dipole antenna, the resonant frequencies can be expressed as (2.10)

$$f_n = \frac{nc}{2L\sqrt{\epsilon_{\text{eff}}}}, \quad n = 1, 3, 5, \ldots \tag{2.10}$$

where L is the effective electrical length of the dipole and ϵ_{eff} is the effective dielectric constant. The fundamental mode ($n = 1$) corresponds to a half-wavelength resonance, while higher-order modes ($n = 3, 5$) provide additional resonant points.

Loop antennas follow a similar principle, with modal resonances given by (2.11)

$$f_m = \frac{mc}{\pi D\sqrt{\epsilon_{\text{eff}}}}, \quad m = 1, 2, 3, \ldots \tag{2.11}$$

where D is the loop diameter. The first-order mode ($m = 1$) corresponds to the λ resonance, and the second-order mode ($m = 2$) to the 2λ resonance.

When these modal resonances are appropriately spaced and impedance-matched, their responses merge to form a continuous wideband characteristic. This principle of mode combination and multi-path resonance is widely applied in modern wideband and ultra-wideband antenna designs.

The degree of overlap between multiple resonant frequencies directly determines the achievable bandwidth. If the resonant points are placed too close together, their impedance curves merge into a single peak, resulting in limited bandwidth improvement. Conversely, if the resonances are spaced too far apart, the antenna exhibits fragmented responses with gaps in between, leading to discontinuous operation.

The optimal condition occurs when adjacent resonant points are positioned such that their impedance curves smoothly connect with each other. In this case, the combined response produces a broad and continuous bandwidth, which may extend to the UWB regime. This process can be interpreted as a form of "multi-point optimization," where structural parameters, parasitic elements, or loading techniques are carefully adjusted to control the frequency distribution of resonant points.

In practice, this concept underpins many modern wideband antenna designs. By optimizing the placement and coupling of multiple resonances, designers can transform a set of narrowband responses into a single, wideband impedance characteristic, thereby meeting the stringent requirements of high-data-rate biomedical applications such as WCE.

2.2.3 Definition and Criteria of UWB

UWB communication is formally defined by the Federal Communications Commission (FCC) as a system with either an absolute bandwidth greater than 500 MHz or a fractional bandwidth exceeding 20%. The fractional bandwidth (FBW) is expressed as (2.12)

$$\mathrm{FBW} = \frac{2(f_H - f_L)}{f_H + f_L} \times 100\% \tag{2.12}$$

where f_H and f_L denote the upper and lower cut-off frequencies at which the antenna reflection coefficient meets the -10 dB matching criterion.

In biomedical applications, and in particular in WCE, UWB operation is highly desirable. The large bandwidth enables higher data rates to support real-time image and video transmission, while also providing robustness against frequency detuning caused by the lossy and dispersive nature of biological tissues. Moreover, UWB antennas can simultaneously cover multiple industrial, scientific, and medical (ISM) bands and medical implant communication service (MICS) bands, enhancing compatibility and flexibility in practical deployment.

2.2.4 Relationship Between Multiple Resonances and Bandwidth

The bandwidth limitation of a single resonance has been established in the previous discussion, where the fractional bandwidth is inversely related to the quality factor. By contrast, introducing multiple resonant frequencies provides a systematic approach to bandwidth enhancement. When two or more resonant points are positioned appropriately, their individual impedance responses overlap, leading to a continuous wideband characteristic.

The achievable bandwidth strongly depends on the number, spacing, and coupling strength of the resonances. If the resonant frequencies are too closely spaced, the impedance curves merge into a single narrow peak, resulting in limited bandwidth improvement. Conversely, if they are too widely separated, the antenna exhibits fragmented responses with gaps between passbands. The optimal condition occurs when adjacent resonant points are positioned such that their impedance loci smoothly connect with each other, producing a broad and continuous operating band that can extend into the UWB regime.

This principle has been widely applied in antenna engineering. For example, dipole antennas can exploit both the fundamental and higher-order modes to generate multiple resonances, while slot- or arm-loaded configurations can introduce parasitic resonances to extend the bandwidth [14–16]. In each case, the design challenge lies in controlling the distribution and interaction of resonant points to achieve the desired wideband or ultra-wideband performance.

2.2.5 Common Techniques for UWB Implementation

Based on the principle of multiple resonances, a variety of design strategies have been developed to realize wideband and ultra-wideband antennas. Some of the most representative approaches include the following:

- **Loading techniques**: Additional resonances can be introduced by incorporating parasitic elements such as arms, loops, stubs, or shorting pins. These structures effectively create alternative current paths, which generate supplementary resonant frequencies and extend the overall bandwidth.

- **Slotting and etching**: Cutting slots into the radiator or the ground plane alters the surface current distribution, thereby exciting multiple modes. Depending on the slot geometry and location, this method provides a simple yet effective means of achieving bandwidth enhancement.
- **Stacked structures**: Employing multiple radiating layers or substrates in a stacked configuration allows strong modal coupling between elements. The resulting interaction of resonances from different layers produces a much broader impedance bandwidth compared to a single-layer design.
- **Conformal geometries**: By bending or wrapping the radiator around a curved surface, the effective current path is lengthened and additional resonances are excited. This approach not only improves bandwidth but also facilitates better integration in applications such as capsule endoscopy, where volumetric constraints are severe.

In summary, these methods all aim to exploit multi-resonant mechanisms through structural modifications. While the specific implementation differs, the underlying principle remains the same: to generate and optimally distribute multiple resonances so that their responses merge into a continuous wideband characteristic.

2.3 Representative Antenna Types for UWB

Having established that UWB performance arises from the controlled superposition of multiple resonances, it is important to examine how these principles are realized in practical radiators. Among the numerous candidates, dipole, folded dipole, and loop antennas represent three canonical families in which multi-resonant mechanisms can be engineered with clear physical interpretation and compact realizations suitable for WCE. The following subsections outline their resonant characteristics and typical bandwidth-extension techniques.

2.3.1 Dipole Antennas

The dipole supports a fundamental half-wavelength resonance and higher-order odd modes. The resonant frequencies can be expressed as (2.13)

$$f_n = \frac{nc}{2L\sqrt{\varepsilon_{\text{eff}}}}, \quad n = 1, 3, 5, \dots \tag{2.13}$$

where L is the effective electrical length, ε_{eff} is the effective dielectric constant, and c is the speed of light. The fundamental mode ($n = 1$) corresponds to the $\lambda/2$ dipole, while higher-order modes ($n = 3, 5$) provide additional resonances. UWB behavior is obtained by merging these modal resonances or by introducing parasitic elements and stubs to generate supplementary resonances. In WCE applications, dipoles are attractive for their geometric simplicity and predictable detuning under tissue loading.

2.3.2 Folded Dipole Antennas

Folding increases the effective current path and input resistance, thereby broadening the matching window. The input resistance of a folded dipole with N arms is approximately

$$R_{\text{in}} \approx N^2 R_{\text{dipole}} \tag{2.14}$$

where R_{dipole} is the radiation resistance of a conventional half-wave dipole. This relationship illustrates why folded structures generally provide wider impedance bandwidth and improved matching tolerance compared with a single dipole.

A more rigorous derivation can be obtained by modeling the folded arms as parallel transmission lines. In this case, each arm pair exhibits a characteristic impedance Z_t, expressed as

$$Z_t = j\eta_0 \tan\left(\frac{\beta l}{2}\right) \tag{2.15}$$

where η_0 is the intrinsic impedance of free space and β is the propagation constant. The characteristic impedance governs the current distribution among the arms, which in turn leads to the effective input resistance scaling described above.

In practice, folded dipoles allow resonance at lower frequencies without proportionally increasing the physical length, while maintaining radiation efficiency. These properties make them particularly attractive for miniaturized and wideband designs in WCE, where both impedance stability and volume efficiency are critical.

2.3.3 Loop Antennas

Loop antennas naturally support resonant modes determined by their circumference. The fundamental resonance is approximately

$$f_m = \frac{mc}{\pi D\sqrt{\varepsilon_{\text{eff}}}}, \quad m = 1, 2, 3, \ldots \tag{2.16}$$

where D is the loop diameter. The first-order mode ($m = 1$) corresponds to a λ-mode, and the second-order mode ($m = 2$) to a 2λ-mode. These modes can be tuned or coupled using slotting, parasitic loops, or capacitive loading to achieve UWB performance. Loop geometries are advantageous in WCE because they efficiently utilize the capsule's circumference and provide robust multimode operation under dielectric loading.

2.3.4 Summary and Transition

In summary, dipole, folded dipole, and loop antennas represent three canonical routes to UWB operation: dipoles exploit fundamental and higher-order modes, folded dipoles leverage impedance transformation and path extension, and loops utilize natural multimode behavior along their perimeter. Each type offers unique benefits for WCE applications, and the integration of these principles motivates the conformal hybrid antenna design presented in this chapter.

2.4 Theoretical Foundation

The proposed antenna combines features of dipole, folded dipole, and loop geometries. From an equivalent-circuit perspective, each of these canonical structures can be modeled by a resonant RLC branch, where R accounts for radiation and ohmic losses, and L and C represent the stored magnetic and electric energies associated with the current distribution. A resonance occurs when the reactive terms cancel, corresponding to the general condition $\omega_0 = 1/\sqrt{LC}$. This equivalence links the physical standing-wave modes on the antenna to lumped-element resonance behavior.

The dipole contribution, expressed in Eq. (2.13), originates from the standing-wave requirement that the effective electrical length corresponds to odd multiples of half wavelengths. Physically, this means that a $\lambda/2$ current distribution produces the fundamental resonance, while $3\lambda/2$ and $5\lambda/2$ modes create higher-order resonances. These multiple resonances appear as distinct valleys in the input reflection coefficient and establish the multimode foundation of the proposed wideband response.

The folded dipole effect, summarized in Eq. (2.14), arises from the redistribution of current among parallel arms. Although the radiated power remains nearly constant, the current division increases the effective input resistance, thereby broadening the matching window. This transformation does not introduce additional resonant frequencies but ensures that multiple resonances are more effectively matched to a 50 Ω system. As a result, folded geometries play a stabilizing role in wideband operation.

Loop antennas, whose resonance relation is given in Eq. (2.16), satisfy the condition that the perimeter length equals integer multiples of the guided wavelength. The fundamental λ mode and higher-order 2λ, 3λ modes each provide distinct resonant points. Unlike dipoles, which support only odd-order resonances, loops naturally yield both odd- and even-order modes. This property enriches the modal spectrum of the antenna and further contributes to ultra-wideband performance. In a conformal capsule configuration, the loop geometry also makes efficient use of the capsule perimeter.

When combined, the overall input impedance of the hybrid antenna can be expressed as the summation of resonant branches:

$$Z_{\text{in}}(\omega) = \sum_{i=1}^{N_{\text{dipole}}} Z_{\text{dipole,i}}(\omega) + \sum_{j=1}^{N_{\text{folded}}} Z_{\text{folded,j}}(\omega) + \sum_{k=1}^{N_{\text{loop}}} Z_{\text{loop,k}}(\omega). \tag{2.17}$$

This formulation reflects the fact that the proposed structure is realized as a continuous conductor, where multiple standing-wave modes coexist along the same current path. Because their impedances add along this shared path, the series RLC interpretation is more accurate than a parallel model, which would instead imply multiple independent current channels connected directly at the feed.

Finally, the reflection coefficient can be expressed as

$$S_{11}(\omega) = 20\log_{10}\left|\frac{Z_{\mathrm{in}}(\omega) - Z_0}{Z_{\mathrm{in}}(\omega) + Z_0}\right|, \tag{2.18}$$

where $Z_0 = 50\ \Omega$ is the reference impedance. Each modal branch contributes a dip in the S_{11} response, and the overlap of these dips produces a continuous wideband or ultra-wideband characteristic. This theoretical framework explains why integrating dipole, folded dipole, and loop features into a conformal design leads to the ultra-wideband behavior validated in subsequent sections.

2.5 Research Gaps and Thesis Positioning

Based on the critical review in this chapter, three major research gaps are identified for wireless capsule endoscopy (WCE) antennas.

2.5.1 Co-design under in-body constraints

Most existing WCE antenna studies optimise impedance matching and bandwidth, yet the electrically small form factor and highly lossy tissues fundamentally reduce radiation efficiency and increase detuning sensitivity. As a result, wide impedance bandwidth alone does not necessarily translate into robust in-body performance, particularly when the antenna is constrained by capsule geometry and tissue loading varies along the gastrointestinal tract. A clear gap therefore exists in jointly optimising *compact size*, *wideband operation*, and *in-body efficiency/robustness* using consistent evaluation metrics and realistic validation environments.

2.5.2 Practical capsule-scale MIMO

MIMO has the potential to improve link reliability and channel capacity under severe fading and orientation uncertainty; however, implementing multiple antennas inside a capsule-scale platform remains challenging due to limited inter-element spacing, strong near-field coupling in high-permittivity media, and correlated radiation patterns. The literature lacks a generalisable miniaturisation and integration strategy that can simultaneously (i) create internal space for multiple radiators without changing the capsule outer geometry, and (ii) maintain low envelope correlation and adequate isolation across a wide operating band. This gap motivates a technical pathway to enable practical MIMO in WCE rather than demonstrating isolated multi-antenna prototypes.

2.5.3 Transparent antenna integration

Transparent antennas have been reported in wearable and display-integrated systems, but WCE introduces a distinctive integration constraint: the antenna must share the frontal area with the camera and illumination while maintaining predictable optical transmittance and RF performance. Prior works often demonstrate a single mesh geometry or a single transparency level, with limited frequency-aware modelling of conductivity and insufficient discussion of how conductivity degradation over time may impact matching and efficiency. A quantitative transparency–conductivity framework, together with a discussion of performance trade-offs and stability, is therefore needed to enable repeatable transparent antenna design for camera-window integration.

To address these gaps, Chapter 3 develops a conformal ultra-wideband antenna to achieve wideband operation within the capsule geometry while improving robustness under in-body loading. Chapter 4 introduces a miniaturisation strategy to enable dual-element MIMO integration with low correlation and adequate isolation. Chapter 5 establishes a transparency–conductivity mapping for inkjet-printed meshes and demonstrates a transparent antenna suitable for camera-constrained WCE platforms.

CHAPTER 3

Conformal antenna for WCE

3.1 Antenna and Capsule

3.1.1 Capsule Dimension

In the current research phase, massive articles have underscored the significance of the capsule dimension. As indicated in [17–20], to enhance comfort and swallowability, the researchers limited the size of the capsule to approximately 11mm × 25mm. Considering the size of the antenna and the capsule, in this study, the size of the external capsule is designed as 25mm × 11mm, as Fig. 3.1(a). The capsule's enclosure comprises three components: the upper lid, the body shell, and the lower lid. The upper and lower lids are hemispherical, each with a radius of 5.5 mm. In contrast, the body shell is cylindrical, with the same radius of 5.5 mm and a height of 14 mm. The entire capsule maintains a uniform thickness of 0.5 mm. Moreover, for simulation accuracy, two blocks were positioned inside the capsule: one block of FR4 material with dimensions of 5mm × 5mm × 1.6mm to simulate the substrate, and another copper block measuring 4.5mm × 4.5mm × 35µm, representing the PCB.

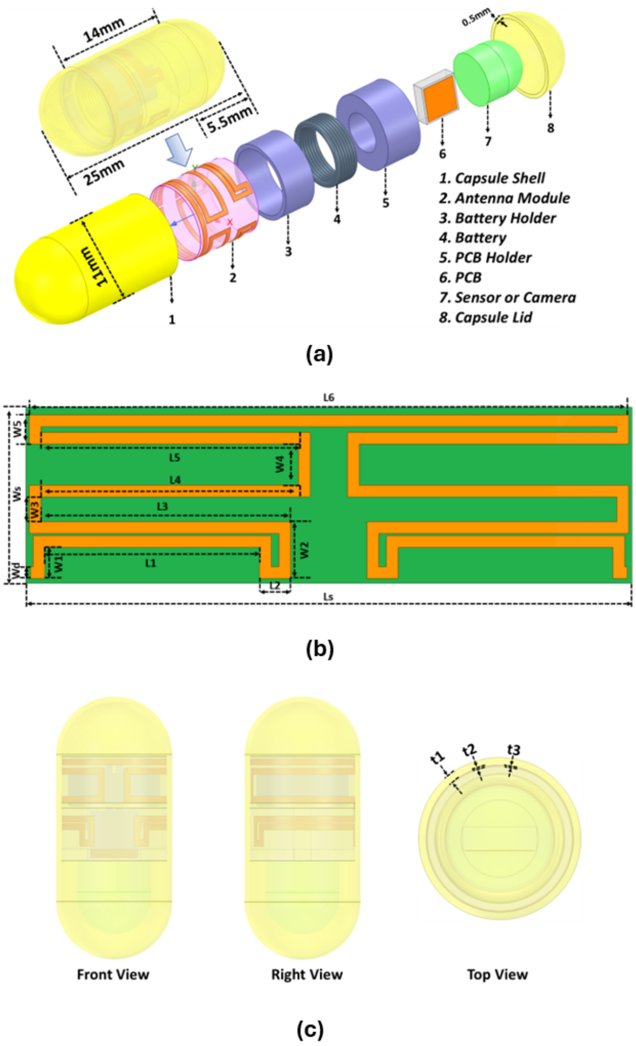

Figure 3.1: (a)Schematic overview of the proposed WCE system. (b)Planar view of antenna module. (c)Front, right and top view of the proposed WCE system

3.1.2 Material and Shape of Antenna

The wide bandwidth and miniaturization of the antenna are mainly affected by two aspects. One is the antenna design, and the other is the selection of the dielectric board material. From the perspective of antenna design, conformal antennas have many advantages. First, conformal antennas can be attached to the outer or inner wall to increase the electrical length as much as possible by designing a meandering path in a limited space to increase the antenna's bandwidth. In addition, in a complex meandering path, the antenna may generate multiple resonance modes that operate at different frequencies to increase the bandwidth of the antenna. The planar geometry of the antenna is depicted in Fig. 3.1(b), with corresponding parameters detailed in Table 3.1. Positioned on the inner wall of the capsule shell, the antenna exhibits lateral symmetry. Moreover, the effective length and area of the antenna are augmented via a meandering design, enhancing the antenna's bandwidth. Within the planar model, the antenna with substrate exhibits a total length of 30.5mm and a width of 9mm, adhering to the standard industrial copper model thickness of 35µm.

Table 3.1: CAPSULE LOOP CONFORMAL ANTENNA PARAMETERS

$L_S = 31\,\text{mm}$	$L_4 = 13.175\,\text{mm}$	$W_2 = 2.9\,\text{mm}$
$W_S = 9\,\text{mm}$	$L_5 = 13.175\,\text{mm}$	$W_3 = 1.2625\,\text{mm}$
$L_1 = 10.981\,\text{mm}$	$L_6 = 30.65\,\text{mm}$	$W_4 = 2.1\,\text{mm}$
$L_2 = 1.594\,\text{mm}$	$W_1 = 1.585\,\text{mm}$	$W_5 = 1.4875\,\text{mm}$
$L_3 = 12.775\,\text{mm}$	$W_d = 0.6\,\text{mm}$	$t_1 = 0.5\,\text{mm}$
$t_2 = 35\,\mu\text{m}$	$t_3 = 0.04\,\text{mm}$	

On the other hand, the material of the substrate is also a crucial factor affecting the bandwidth. In the design of conformal antennas, the choice of substrate material must combine flexibility and high dielectric constant to accommodate non-planarity while allowing higher bandwidth. In studies [10–12, 15], two materials, Rogers 6010 and Rogers Ultralam were mainly used. However, despite the high dielectric constant of these materials, they could not meet the flexibility of the manufacturing process, which means that this material is not suitable for the design of a conformal antenna. In [21], the authors suggest using Polyimide($\varepsilon_r = 3.5$, tan$\delta = 0.008$) as the substrate. This is because Polyimide can be easily bent to match the dimensions of the capsule's inner wall. Moreover, its exceptional biocompatibility and chemical stability make Polyimide an ideal choice for the capsule shell and substrate.

3.1.3 Simulation and Measurement Setup

The research primarily comprises two main stages. Initially, the antenna prototype will be designed within a homogeneous phantom box. After that, this antenna will be optimised within a human model. Considering simulation time and efficiency, the homogeneous phantom box is configured as a three-layered cylinder in High-Frequency Structure Simulator (HFSS). This cylinder, consisting of muscle, fat and skin from the inside out, has 250mm, 5mm and 3mm thicknesses, respectively, as

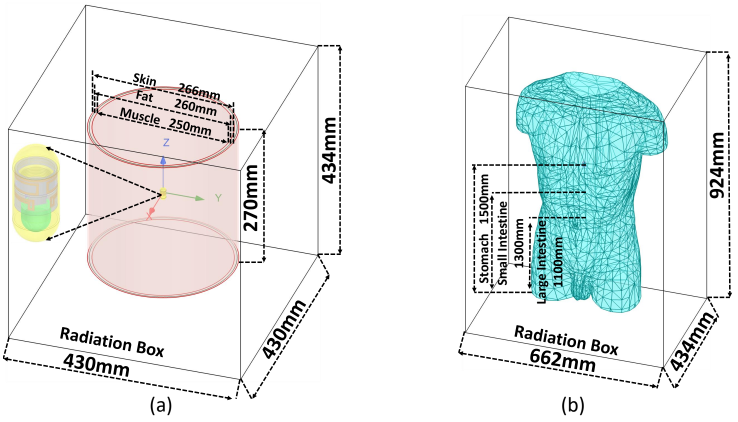

Figure 3.2: Simulation setups of the proposed antenna. (a) Homogeneous simulation setup. (b) Heterogeneous simulation setup

shown in Fig. 3.2 (a). Moreover, as the permittivity and dielectric dissipation factor of the human body varies with frequency, the permittivity (ε_r) and dielectric dissipation factor (tanδ) ranging from 100 MHz to 10 GHz as cited in [22] were referred to approximate the value in the parameters of the three human tissues. Throughout the simulation, the antenna and capsule shell was placed at the centre of the homogeneous phantom box and at the (0, 0, 0) position of the *O-xyz* coordinates.

In Fig. 3.2 (b), the optimized antenna model will be placed in a high-precision human body model for parameter analysis. The antenna will be positioned above the origin of the coordinate system O-xyz at distances of 1500mm, 1300mm, and 1100mm to simulate and analyze the WCE in the stomach, small intestine, and large intestine, respectively.

3.2 Result and Discussion

The optimization of a conformal antenna in a homogeneous phantom box and the variation of the reflection coefficient are presented in Fig. 3.3. It is obvious that the operating frequency of Step 1 in Fig. 3.3 (a) is significantly higher than 915MHz. To lower the resonant frequency, the electrical length of the antenna can be increased by folding and bending the current path on its surface. By extending the folded portion in Step 1, the operating frequency of the antenna decreases as shown in Step 2. However, this results in the formation of two bands, leading to a shorter

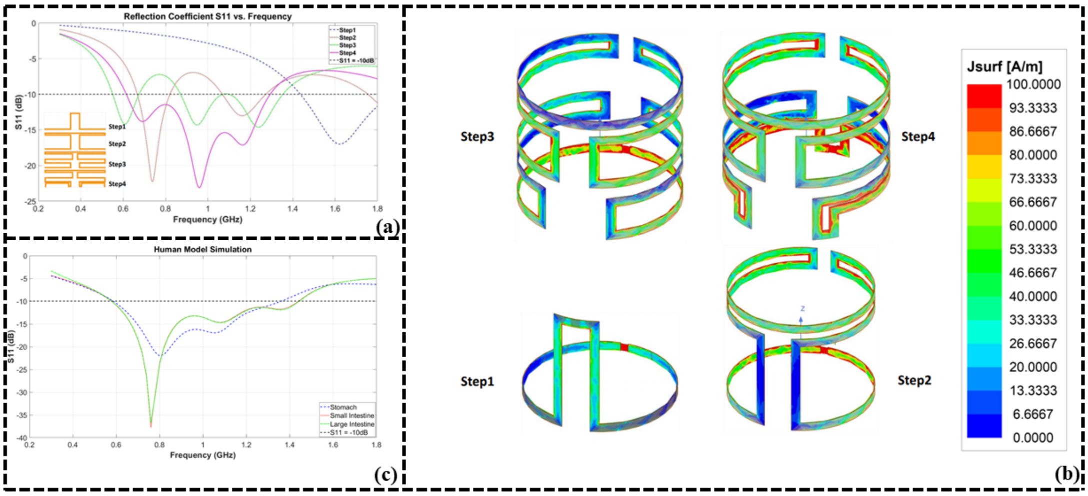

Figure 3.3: (a) Designing steps and respective reflection coefficients. (b) Current density distributions of designing steps. (c) Reflection coefficient in the stomach, small intestine and large intestine.

bandwidth.

In Step 3, the length of the antenna is further extended beneath the previous folded structure to increase the bandwidth. Nonetheless, some impedance mismatches between the two structures cause a portion of the bandwidth to exceed -10 dB. Hence, in Step 4, reverse vector current technology is utilized to create mirrored structures on both sides of the existing structure, optimizing impedance matching and enhancing the bandwidth. Fig. 3.3 (b) illustrates the S11 parameter obtained from the optimized antenna model placed within a simulated real human environment. The impedance bandwidth (-10 dB) in the stomach was 0.59 GHz - 1.36 GHz (770 MHz), while in the small intestine and large intestine, it was 0.58 GHz - 1.44 GHz (860 MHz). In each scenario, the operational frequency range is broadened to cover the useful license-free bands of 868 – 868.6 MHz and 902 – 928 MHz. This enables the proposed antenna system to function effectively in various implantation sites for diverse applications. Additionally, it provides a high channel capacity, facilitating high data transmission. The simulated normalized radiation patterns of the suggested antenna at $\phi = 0^o$ and $\phi = 90^o$ in the stomach, small intestine, and large intestine are depicted in Fig. 3.4 (a)(b)(c). The simulated peak

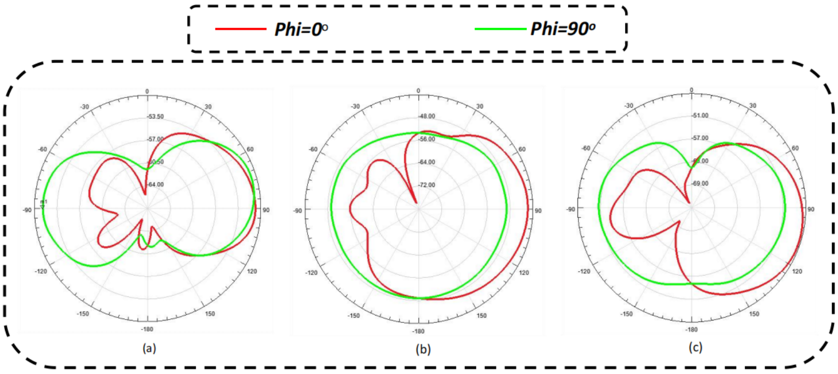

Figure 3.4: Radiation Pattern

gain inside the stomach, small intestine, and large intestine were -50.7, -41.7, and -45.4 dBi repectively.

Table 3.2: COMPARISON OF STOMACH IMPLANT ANTENNAS AT 915 MHz

Ref	**Freq/MHz**	**Size/mm^3**	**Bandwidth/MHz**	**Gain/dBi/stomach**
My work	915	10.98=30.4x9x0.04	770 (96.25%)	-50.7
[23]	915	107=53.5x10x0.2	185 (20.21%)	-28.7
[24]	915	2090.73=πx5.5x5.5x22	170 (18.57%)	-24
[25]	915	9.31=18x12x0.0431	214 (23.38%)	Not mentioned
[26]	915	8=32x10x0.025	104 (11.36%)	-28.75
[27]	915	106=29.8x14x0.254	85 (9.28%)	Not mentioned
[28]	915	182=28x12x0.5	670 (73.22%)	-16.8

Table 3.2 provides a comparison of the proposed UWB antenna system with several previously reported implantable antennas. Notably, the proposed antenna excels in compactness and exhibits an impressive bandwidth, making it to withstand detuning while also being well-suited for high data rate transmission.

3.3 Safety Evaluation

For safety concern, the peak Specific Absorption Rate (SAR) values were calculated in accordance with the IEEE C95.1-1999 and C95.1-2005 standards. SAR can be calculated as follows:

$$SAR = \sigma E^2/2\rho \qquad (3.1)$$

where E, σ, and ρ represent electrical field magnitude, conductivity, and mass density

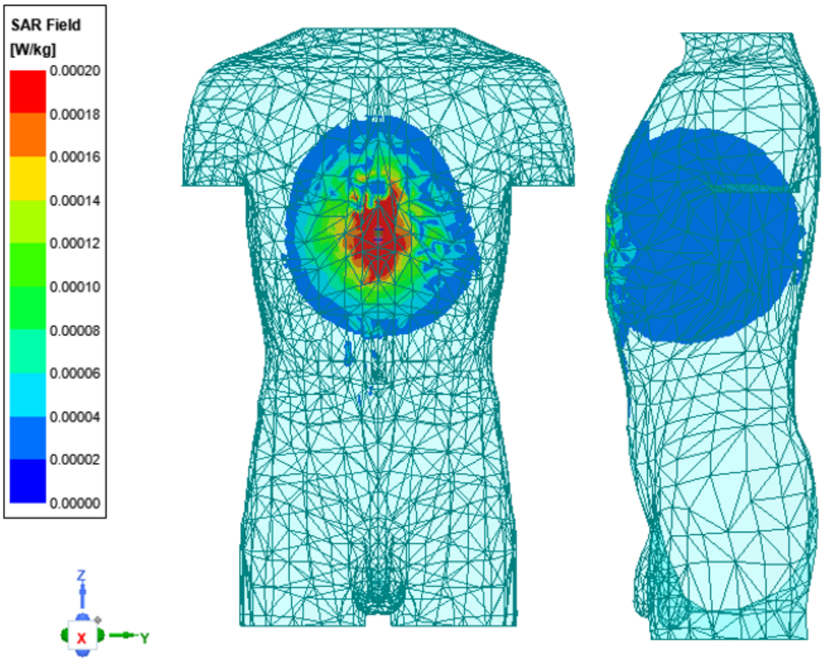

Figure 3.5: Simulation of the SAR of the antenna at 915MHz over 1-g of tissues

of the tissues respectively [29]. In figure 3.5, the 1-g SAR is evaluated in human model phantom. When the suggested antenna was simulated to deliver 25 μW, the simulated maximum 1-g average SAR values were 0.00020 W/kg at 915MHz. The SAR values are under the IEEE limits. Thus, this design is suitable for WCE application in these frequencies.

3.4 Link Budget Analysis

Link budget analysis is used to translate antenna-level performance (e.g., gain and matching) into a system-level communication capability, i.e., the achievable transmission distance under a given data rate requirement. The link margin (LM) is defined as the difference between the *available received power* and the *required received power* at the receiver. A positive margin (LM $>$ 0 dB) indicates that the received signal power is sufficient to meet the receiver sensitivity requirement with additional robustness against fading, detuning, and shadowing in practical environments. Following [23], the link margin can be expressed as

$$\mathrm{LM} = A_p - R_p, \tag{3.2}$$

Table 3.3: LINK BUDGET PARAMETERS AT 915 MHz

Specification	**Variable**	**Value**
Operating frequency (MHz)	f	915
Transmit power (dBm)	P_t	-16
Temperature (K)	T_0	293
Transmitting antenna gain (dBi)	G_t	-45.93
Receiving antenna gain (dBi)	G_r	2.1
Path loss (dB)	L_p	Distance dependent
Available received power (dB)	A_p	Distance dependent
Required received power (dB)	R_p	Data-rate dependent
Margin (dB)	$A_p - R_p$	Fig. 3.6

where A_p denotes the available received power (in dB) and R_p denotes the required received power (in dB).

The required received power can be written as

$$R_p(\text{dB}) = E_b/N_0 + KT_0 + B_r, \tag{3.3}$$

where E_b/N_0 is the required energy-per-bit to noise spectral density ratio (in dB), K is the Boltzmann constant, T_0 is the absolute temperature (K), and B_r is the transmission bit rate (Mb/s). Equation (3.3) highlights that increasing the bit rate raises the required received power, thereby reducing the achievable communication distance for a fixed transmit power and antenna configuration.

The available received power is given by

$$A_p(\text{dB}) = P_t + G_t + G_r - L_p - P_L, \tag{3.4}$$

where P_t is the transmit power (dBm), G_t and G_r are the gains of the transmitting and receiving antennas (dBi), respectively, L_p is the path loss (dB), and P_L is the polarisation mismatch loss (dB).

The distance-dependent path loss is modelled as

$$L_p(\text{dB}) = 20\log_{10}\left(\frac{4\pi d}{\lambda}\right) + 10\gamma\log_{10}\left(\frac{d}{d_0}\right) + S_e, \tag{3.5}$$

where d is the separation distance, λ is the wavelength, γ is the path-loss exponent,

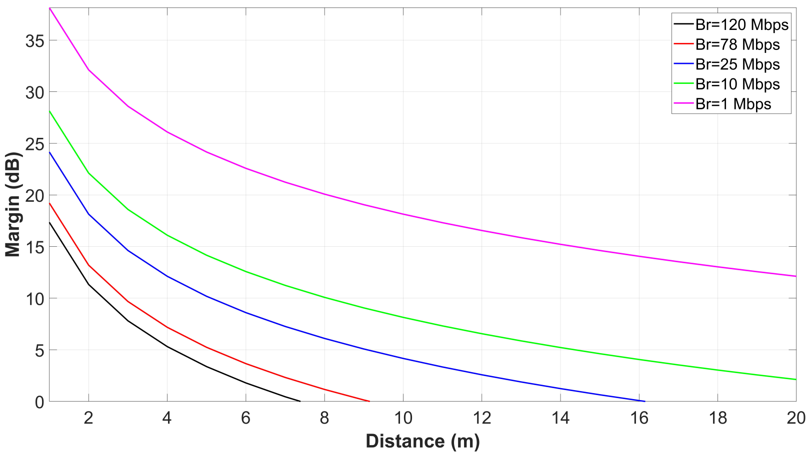

Figure 3.6: Link margin versus distance at 915 MHz for different data rates.

and S_e represents the log-normal shadowing term with standard deviation σ.

Table 3.3 summarises the parameters used in (3.3)–(3.4). As shown in Fig. 3.6, higher data rates lead to a faster reduction in link margin with distance because R_p increases with B_r. For data rates of 1, 10, 25, 78, and 120 Mb/s, the link margin remains above 0 dB up to approximately 20, 14, 8, 6 m, respectively. For indoor bio-telemetry scenarios, a communication range of 6–8 m is often of interest [26]; therefore, the proposed design provides sufficient margin to support high-throughput WCE telemetry within typical indoor monitoring distances.

3.5 Conclusion

This chapter presented the design, simulation, and experimental validation of a conformal UWB antenna optimized for WCE applications. By integrating the modal characteristics of dipole, folded dipole, and loop structures within a conformal geometry, the proposed antenna achieved a compact profile of 30.5 mm × 9 mm × 0.04 mm while maintaining a fractional bandwidth of 96.25%. The measured results verified stable impedance matching and radiation performance in multiple implantation scenarios, confirming the robustness of the design under realistic biological conditions.

Despite its promising performance, several limitations remain. The overall antenna volume, although conformal to the capsule wall, still occupies a considerable portion of the internal space, restricting the integration of additional modules or multiple antennas. Furthermore, the realized gain is relatively low due to lossy tissue loading and limited aperture size. These constraints motivate continued efforts toward antenna miniaturization and multi-antenna configurations to further improve channel capacity within confined capsule environments.

To address these challenges, the next chapter introduces a miniaturized dual-element multiple-input multiple-output (MIMO) antenna system. Through the use of dielectric hollowing and decoupling techniques, the design aims to achieve reduced volume, wideband impedance stability, and sufficient isolation between elements, thereby extending the conformal UWB framework toward high-capacity capsule communication.

CHAPTER 4

The Design of Minimization and MIMO Configuration

The previous chapter presented the design and realization of a conformal UWB antenna for WCE. While the proposed single-element antenna achieved wide impedance bandwidth and stable performance under tissue loading, its structure still occupied a considerable portion of the capsule's inner wall. This space constraint limits the integration of additional functional components such as imaging modules, power sources, and communication circuits. Moreover, a single-element configuration cannot fully exploit the spatial diversity of the in-body propagation environment, which is crucial for improving data transmission capacity and link stability. To address these challenges, this chapter focuses on the development of a miniaturized conformal multiple-input multiple-output (MIMO) antenna system that combines compactness, ultra-wideband characteristics, and spatial diversity.

4.1 MIMO Advantages in the WCE Environment

The propagation environment inside the human gastrointestinal (GI) tract is highly complex. The capsule constantly changes its orientation and position as it moves through the GI tract, and its surrounding tissues present nonuniform dielectric properties and high absorption. These factors result in severe multipath propagation, polarization mismatch, and signal fading, which significantly degrade communication reliability.

MIMO technology provides an effective solution to these problems. By employing multiple radiating elements with decorrelated field distributions, MIMO systems exploit spatial diversity to counteract multipath fading and maintain a stable link under dynamic conditions. Through spatial multiplexing, independent data streams can be transmitted simultaneously, effectively increasing channel capacity without requiring additional frequency resources—a critical factor for real-time high-definition image and video transmission in WCE. Furthermore, the inherent redundancy of MIMO improves robustness against deep fading and detuning caused by tissue loading, making it a natural complement to the UWB concept established in the previous chapter. Together, UWB and MIMO technologies offer the potential for high-capacity, low-latency, and highly reliable communication within the constrained and lossy in-body channel.

4.2 Literature Review on MIMO and UWB Antennas for WCE

Ensuring high-channel capacity for high-data-rate transmission of images and videos to cloud servers is a complicated task [10, 30, 31]. Moreover, antenna frequency detuning poses a significant challenge, due to the complex electromagnetic (EM) properties of the human body's tissues and fluids along the GI tract [10, 32].

This issue is further aggravated by the dynamic movements and changes in the patient's posture. These variations can alter the effective impedance seen by the antenna, resulting in a shift in the antenna's operating frequency [33]. In [8, 12, 15], researchers have adopted long-arm spiral and open-slotted designs to adjust the electrical length, and enhance the bandwidth. However, it should be noted that the designs in [8, 12, 15] are single-input-single-output (SISO) topologies. SISO systems provide lower data throughput and are more susceptible to signal fading, leading to potential drops in reliability and performance. To address these challenges, the integration of both MIMO and UWB technologies has surfaced as a promising solution [34]. It offers higher data rates, robustness against multipath fading and frequency detuning mitigation [4, 19, 34].

Recent studies in [35–38] have discussed the integration of technologies such as UWB or MIMO for implantable antenna application. In [35], a compact two-module MIMO antenna system utilizing a grounded meander resonator and open slots achieved significant miniaturization (5.35 mm × 6.2 mm × 0.12 mm), offering a FBW of 13.1% (320 MHz) and 28 dB isolation. In [36], authors introduced a patch antenna based on a circular structure with symmetrical arc-shaped slots, achieving a FBW of 33.9% (355 MHz - 500 MHz) and compact dimensions ($0.13 \times \pi \times 5.65^2$ mm^3). In [37], a spiral symmetry structure embedded into the ground is used to achieve a bandwidth from 320 MHz to 460 MHz, with a FBW of 25.9% and a modest volume (22 mm × 12 mm × 0.635 mm). A quad-element MIMO antenna system detailed in [38] comprises semi-circular meander radiators, achieving a FBW of 38.26% (355 MHz - 523 MHz) with dimensions of 13.5 mm × 13.5 mm × 0.13 mm.

However, these reported MIMO antenna systems employ planar configurations. Such planar antenna structures occupy considerable space inside the capsule, limiting the available volume for other essential components. Conformal designs, presented in [39] and [40], have been introduced to address space constraints for WCE applications. In [39], researchers presented a dual planner helical radiator achieving a FBW of 15.1% (2.26 GHz - 2.63 GHz) with an antenna size of 34.65 mm^3. In [40], authors utilized a conformal-rectangular patch antenna combined with a curved slotted structure, attaining a FBW of 12.63% (0.84 GHz - 0.96 GHz) and a size of 29.91 mm^3. Nevertheless, while these innovative conformal designs aim to minimize space occupation, they often do not achieve UWB characteristics and face a trade-off between size and bandwidth.

This chapter presents a novel conformal dual-element MIMO antenna system for WCE applications. The MIMO antenna elements exhibit UWB characteristics, from 0.61 GHz to 1.51 GHz with 84.91% FBW. This design has a volume of 30.5 mm × 15 mm × 0.04 mm placed on the 11 mm × 26 mm inner wall of the capsule.

The proposed antenna design offers (1) high data transmission and (2) effectively mitigates frequency detuning without compromising on the overall antenna performance or device compactness. To the best of the authors' knowledge, the proposed MIMO antenna model achieves the widest bandwidth among existing MIMO antennas, along with the smallest reported size to date.

4.3 Design Methodology

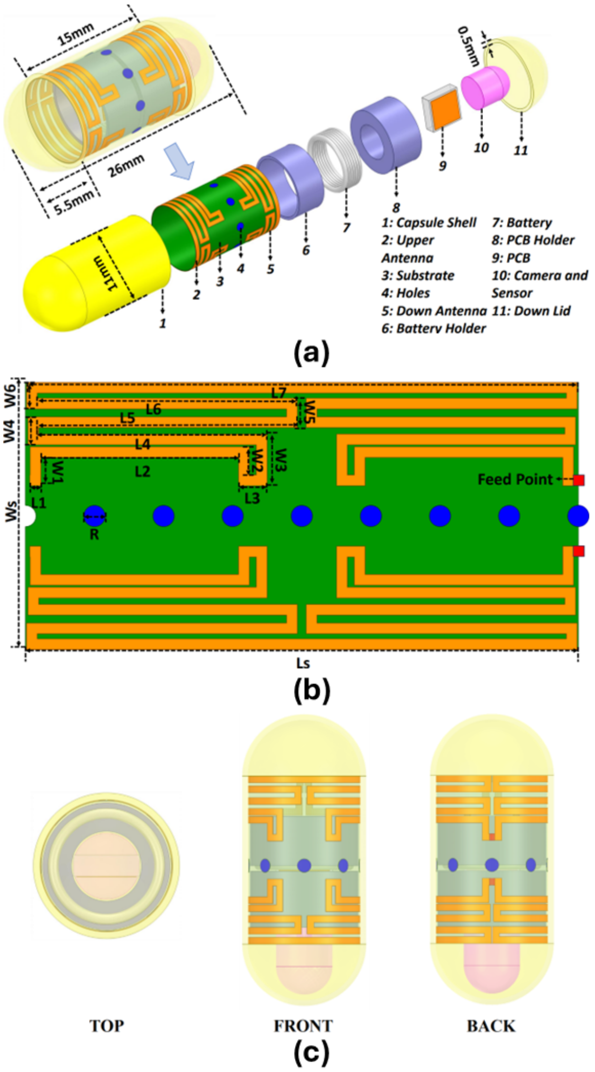

Figure 4.1: (a) The proposed WCE system partial view. (b) Planar antenna structure diagram. (c) Top, front, and back view of WCE model. The geometrical dimension of planar antenna: $L_S = 30.5$, $W_S = 15$, $L_1 = 0.618$, $L_2 = 11.088$, $L_3 = 1.594$, $L_4 = 12.799$, $L_5 = 14.499$, $L_6 = 14.585$, $L_7 = 30.87$, $W_1 = 1.585$, $W_2 = 1.585$, $W_3 = 2.9$, $W_4 = 1.5625$, $W_5 = 2.9$, $W_6 = 1.4875$, $R = 0.6$ (Unit: mm).

The WCE components outlined in this paper are depicted in Fig. 5.9(a). It comprises two antenna elements, four batteries, a camera, sensors, and a Printed Circuit Board (PCB). The all above components are encapsulated in a 3D-printed capsule, made from bio-compatible Polyimide ($\varepsilon_r = 3.5$, tan$\delta = 0.008$). Fig. 5.9(b) illustrates the structure of the two antenna element model in its unfolded condition. The material will bend along the capsule's inner wall and be attached at the feeding point to create a loop. Fig. 5.9(c) displays the proposed WCE model from various viewing angles. This design utilizes a Polyimide substrate with 0.04 mm thickness to achieve compactness and flexibility. The antennas form a minimal volume of 14.384 mm^3. Eight holes are evenly distributed on the substrate between the two antennas to further enhance the impedance matching. This configurations can reduce the local effective permittivity of the substrate to optimize the impedance matching [41].

4.3.1 Simulation Environment

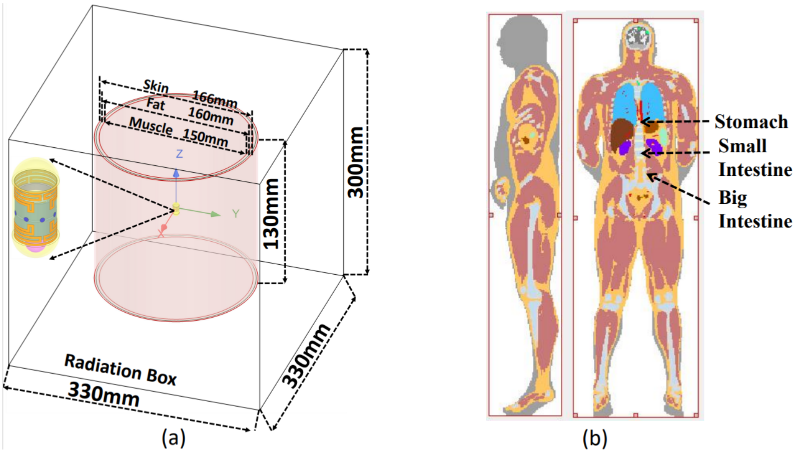

Figure 4.2: Setup of MIMO system simulation. (a) Three-layered cylinder phantom model simulation. (b) Heterogeneous human model simulation.

The proposed antenna model is designed within a phantom model and optimized in a heterogeneous human body model, as illustrated in Fig. 5.11. Initially, we used a phantom model represented by a three-layered cylinder configuration in the High Frequency Structure Simulator (HFSS), as depicted in Fig. 5.11(a). The cylinder, consists of muscle, fat, and skin. The permittivity and dielectric dissipation factor of these tissues vary with frequency [22]. In the next step, the proposed antennas are optimized in a heterogeneous human model in CST Studio Suite (CST), as shown in Fig. 5.11(b). The proposed MIMO antenna system is simulated at different regions of the GI tract.

4.3.2 Evolution Steps

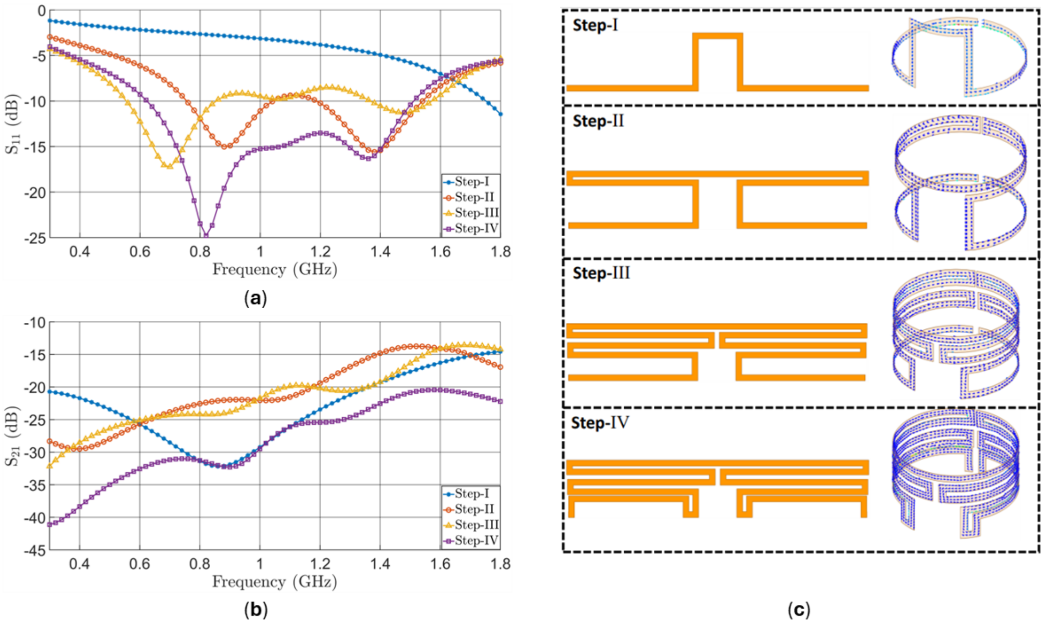

Figure 4.3: (a) The S_{11} with different steps. (b) The S_{21} with different steps. (c) The current distribution with different steps.

In this study, the proposed antenna model goes through four iterative steps to obtain the desired results. Fig. 4.3(a) and (b) show the S-parameters under different steps. As shown in Fig. 4.3(c), Step-I demonstrates that when the antenna consists of a single metal wire with a single bend, its resonant frequency stands at 2.25 GHz. The isolation level between the two antennas is 14 dB. Step-II involves bending and folding the antenna to extend its electrical length. This extension allows current to flow along the newly created radiating components on the surface. As a result, the resonant frequency is reduced. Furthermore, the mirror structure modifies the original design, enhancing the bandwidth. The antenna's operating frequency band covers 915 MHz. However, the impedance matching between 1 GHz and 1.2 GHz remains poor and the isolation is about 13 dB. Step-III involves designing a new mirror-symmetric structure to introduce an additional operating frequency.

Accordingly, the antenna is operating at three frequencies of 0.67 GHz, 1.3 GHz, and 1.45 GHz resulting in an improved overall bandwidth. However, the antenna's self-inductance leads to an impedance mismatch from 0.9 to 1.35 GHz. Therefore, in Step IV, a reverse vector current technique [42] is implemented to decrease the self-inductance and enhance impedance matching in this band. The bandwidth of the fully optimized antenna ranges from 0.61 to 1.51 GHz, with a FBW of 84.91% and an isolation level better than 20 dB.

4.3.3 The Influence of Holes

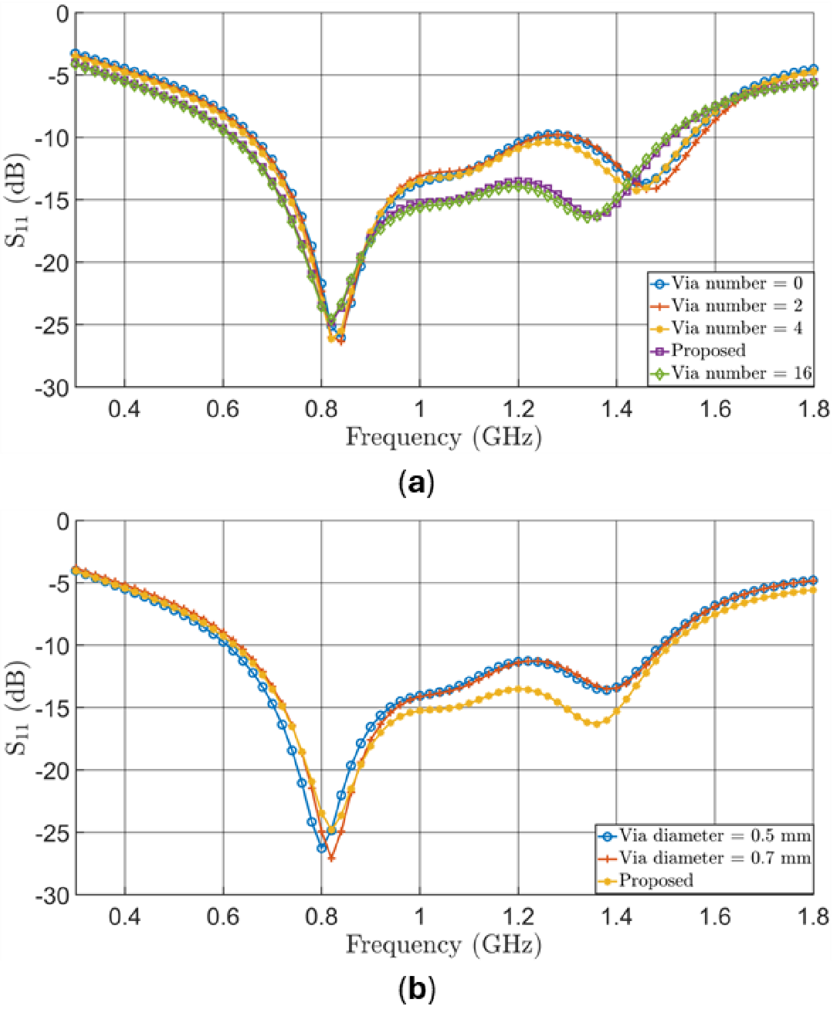

Figure 4.4: (a) Holes numbers effect. (b) Holes diameter effect.

The presence of holes between the antennas effectively reduces the local permittivity of the substrate, forming a synthesized low-dielectric-constant region that alters the electromagnetic characteristics of the structure. As reported by Gauthier *et al.* [43], closely spaced holes can form an artificial medium whose effective permittivity is determined by the hole diameter (d) and center-to-center spacing (p). When the periodicity of the holes is much smaller than the operating wavelength ($p \ll \lambda$), the structure can be modeled quasi-statically, and the synthesized effective permittivity $\varepsilon_{\text{eff, synth}}$ can be approximated by

$$\varepsilon_{\text{eff, synth}} = (1 - V_{\text{r}})\varepsilon_{\text{r,sub}} + V_{\text{r}}\varepsilon_{\text{air}}, \tag{4.1}$$

where V_{r} is the fractional volume removed by the holes, and $\varepsilon_{\text{r,sub}}$ represents the dielectric constant of the unperforated substrate. For a hexagonal or triangular lattice, V_{r} can be expressed as

$$V_{\text{r}} = \frac{\pi d^2}{2\sqrt{3}p^2}. \tag{4.2}$$

Therefore, the synthesized dielectric constant can be tailored through the hole geometry. A higher hole density (larger V_{r}) leads to a lower $\varepsilon_{\text{eff, synth}}$, which increases the phase velocity of electromagnetic waves within the substrate, given by

$$v_p = \frac{c}{\sqrt{\varepsilon_{\text{eff, synth}}}}. \tag{4.3}$$

The reduction in $\varepsilon_{\text{eff, synth}}$ results in a longer guided wavelength λ_g and consequently a broader impedance bandwidth for a given physical antenna length. This mechanism can be interpreted as a localized "dielectric hollowing" effect that decreases the stored electric energy beneath the antenna, thereby reducing the quality factor Q and improving the fractional bandwidth, approximately given by

$$\text{FBW} \propto \frac{1}{Q} \approx \frac{1}{\sqrt{\varepsilon_{\text{eff, synth}}}}. \tag{4.4}$$

Furthermore, local modification of the dielectric constant improves impedance matching between adjacent antenna elements in the MIMO configuration, as the refractive index contrast between the antenna and substrate is reduced. This localized dielectric tailoring provides a controllable trade-off between miniaturization and bandwidth enhancement, making it particularly suitable for implantable conformal

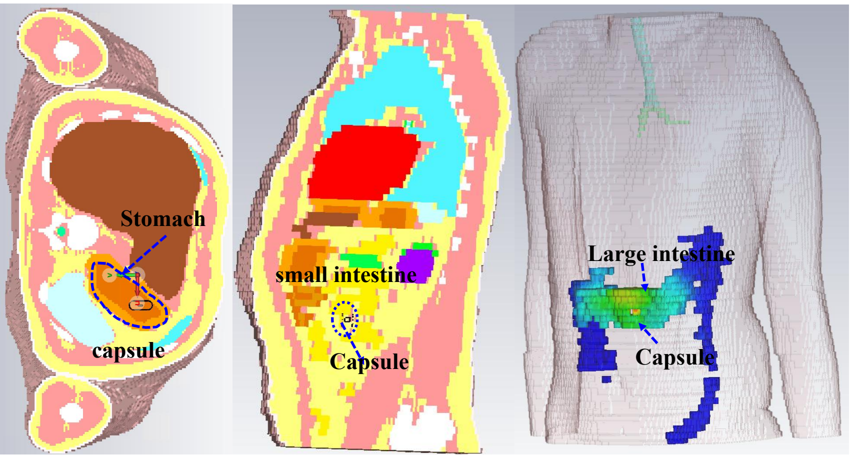

Figure 4.5: The robustness validation in stomach, small, and big intestine.

antenna designs, where both compactness and isolation are essential. Fig. 4.4(a) and (b) show the impact of varying holes number and size on S_{11}. It is noted that the reflection coefficient in the 1.2-1.4 GHz frequency range consistently exceeds -10 dB in the absence of holes between the two antennas. The antenna's S_{11} exhibit minimal change when two holes are arranged between antennas. The reflection coefficient falls below -10 dB when 4 holes are integrated. S_{11} between 1.2 and 1.4 GHz frequency band is further reduced to -13.5 dB using 8 holes arrangement. Additionally, the effect of 16 holes on the S_{11} is investigated. However, the impact is determined to be negligible. Consequently, an arrangement with 8 holes is adopted.

Furthermore, the effect of holes diameter on S_{11} is investigated. Fig.4.4(b) illustrates the direct effect on S_{11} when the holes diameters are 0.5 mm, 0.6 mm (proposed), and 0.7 mm. Holes with diameter of 0.6 mm are found to achieve the best performance in terms of bandwidth.

4.3.4 S-Parameters at Various GI Tract Locations

The human body comprises various biological tissues, each possessing different electromagnetic properties, including dielectric constant and conductivity. The antenna's impedance matching is affected by the surrounding tissue. In Fig. 4.5, the proposed MIMO antenna system is implanted at various locations within a CST heterogeneous human model to simulate realistic scenarios. Fig. 4.6 shows the S_{11} and S_{21} results when the antenna model is implanted at the stomach, small, and big

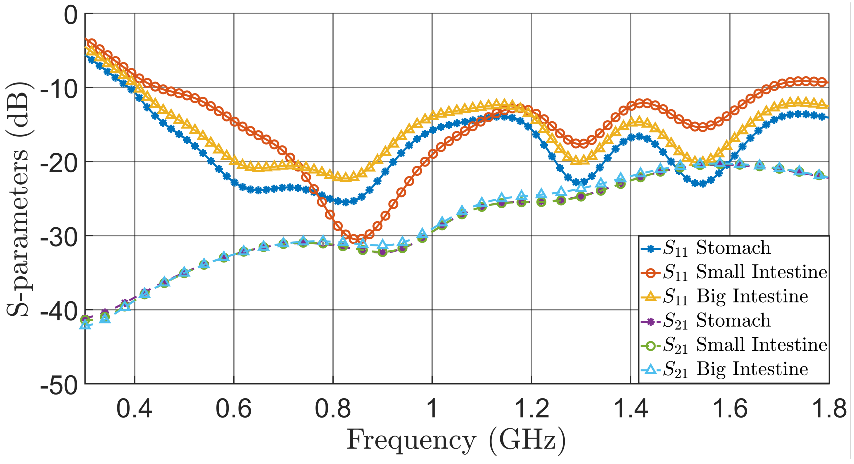

Figure 4.6: The S-parameters at stomach, small, and big intestine.

intestine. The proposed antenna demonstrates UWB characteristics, ranging from 0.4 to 1.8 GHz, when positioned in the stomach. After relocating the antennas from the stomach to the small intestine, the bandwidth narrows to 0.5-1.7 GHz frequency range. However, the lowest reflection coefficients are reached when the antenna moves to the big intestine section. The operating range remains from 0.5 GHz to 1.8 GHz. Regardless of the antenna position inside the GI tract, it consistently maintains UWB characteristics and covers the ISM band.

4.4 Results and Analysis

The proposed antenna design is fabricated using the specified Polyimide substrate to validate the simulated results. Fabricated antennas prototype are shown in both planar and conformal configurations in Fig. 5.12(a). For the antenna's S-parameter and radiation pattern measurements, the entire assembly is then immersed in minced pork, serving as a tissue-equivalent material for the human digestive system.

4.4.1 S-Parameter

The proposed antenna's S-parameters are measured using a Keysight P9374A portable Vector Network Analyzer (VNA), with the antenna elements connected via coaxial cables. A comparison between the simulated and measured S-parameters is shown in Fig. 5.13. The simulated results indicate a working frequency range from 0.61

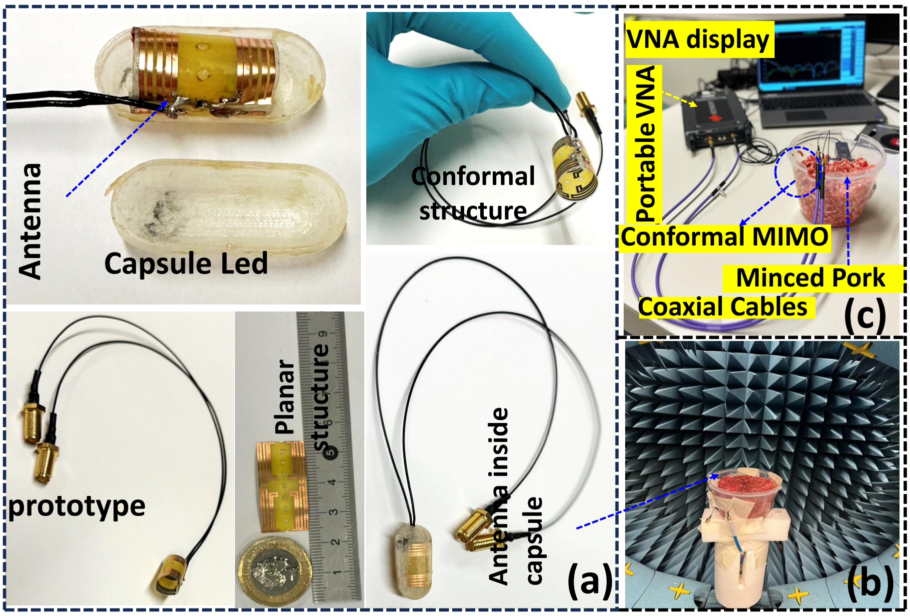

Figure 4.7: (a) The fabricated antenna prototype before and after encapsulating. (b) Setup for Measuring Radiation Patterns. (c) Setup for Measuring S-Parameters.

GHz to 1.51 GHz, a fractional bandwidth (FBW) of 84.91%, and an isolation level better than 20 dB between the two antennas. The measured results demonstrate that the suggested antenna maintains a reflection coefficient below -10 dB across a slightly wider frequency range, from 0.5 GHz to 1.8 GHz, with a similar isolation level. Discrepancies between these results can be attributed to several factors related to the manual assembly and integration process. One of the main challenges arises from the use of the thin Polyimide substrate, which needs to be conformed to the capsule structure during integration. The conforming process may introduce slight deformations, such as substrate stretching or compression, which can affect the antenna's performance, leading to discrepancies between the simulation and measurement. Additionally, potential variations in the positioning and alignment of the antennas and other elements within the capsule and inconsistencies in the manual soldering of the coaxial cables to the antenna elements may also contribute to the observed discrepancies. Furthermore, differences in the dielectric properties between the heterogeneous human model used in the simulation and the actual minced pork used in measurements may also play a role. Despite these factors, the overall performance of the proposed antenna remains consistent with the simulated results, demonstrating its ultra-wideband characteristics and reliability, which confirms its

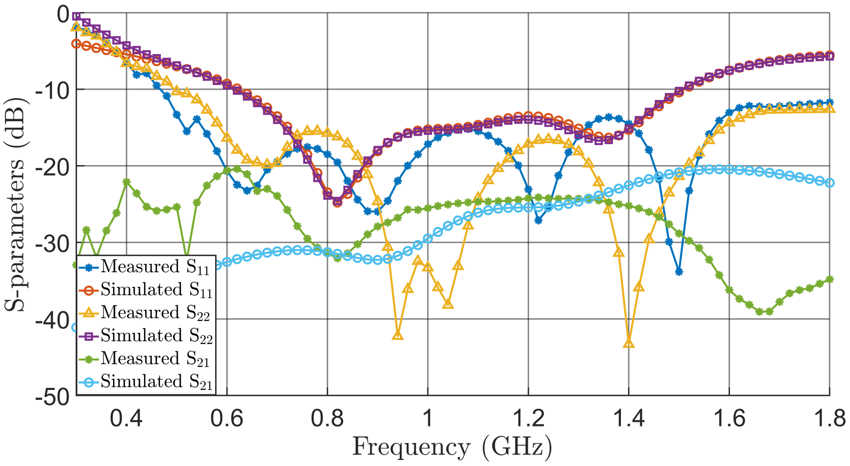

Figure 4.8: Comparison of simulated and measured S-parameters.

suitability for WCE applications.

4.4.2 Radiation Pattern and Gain

The fabricated antenna prototype is measured in an anechoic chamber while immersed in minced pork to validate the antenna radiation performance in the target application, as depicted in Fig. 5.12(b). One port of the MIMO antennas connects to the spectrum analyzer, and the second port terminates with a 50 Ω load. A high-gain horn antenna is used as the transmitting antenna, positioned one meter away from the proposed antenna. The incoming power at the proposed antenna is captured with a 1° angular resolution.

Fig. 4.9(a) presents the simulated and measured 2D radiation patterns at ϕ values of 0° and 90° at 915 MHz. The simulated radiation pattern exhibits a peak gain of -34 dBi, while the measured peak gain is -30.4 dBi. This discrepancy can be attributed to the factors discussed earlier. Despite these differences, the main lobe of the radiation pattern spans from $\theta = 30°$ to 150° and from $\theta = 210°$ to 330° in both simulated and measured results. The 3D radiation patterns of the proposed antenna are illustrated in Fig. 4.9(b) and (c) when antenna 1 and antenna 2 are excited, respectively. Both antennas exhibit similar radiation patterns, with the main lobe oriented along the θ direction (0° - 180°) and the ϕ direction (90° - 270°). This characteristic ensures that the antenna maintains high gain over a wide angular range, enabling efficient transmission and reception of signals through the human

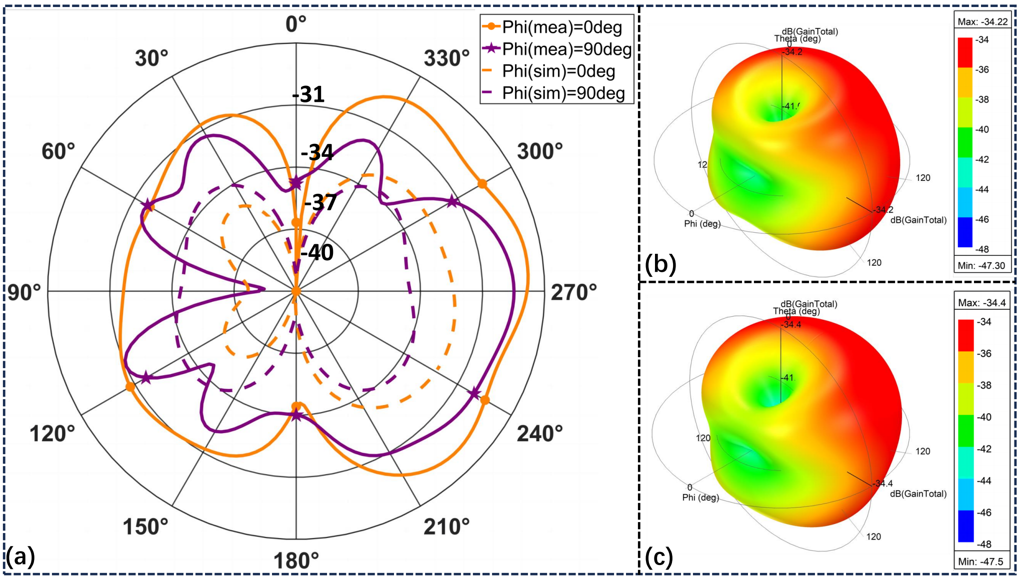

Figure 4.9: (a) The comparison of simulation and measurement radiation pattern. (b) The 3D radiation pattern for antenna1 (c) The 3D radiation pattern for antenna 2.

body, which is crucial for reliable communication in WCE applications.

4.4.3 SAR Evaluation

In WCE applications, the capsule containing the antenna system is ingested by the patient and travels through the GI tract, making it crucial to ensure the EM radiation exposure is within safe limits to prevent potential harm to the patient. SAR is a vital parameter for evaluating the absorption of EM waves by the human body. The IEEE C95.1-2019 standard specifies that the maximum 10 gram averaged SAR should below than 2 W/kg to ensure patient safety [37]. To comprehensively assess the SAR performance of the proposed antenna, numerical simulations are analyzed using the human body model. The capsule with the integrated antenna is implanted within the stomach, small intestine, and large intestine in the simulations to account for various positions of the capsule during its transit through the GI tract. The simulations are performed with an input power of 25 μW, following the guidelines set by ITU-R RS.1346 [25] for implantable medical devices. Fig. 5.15 shows the SAR analysis carried out at the operating frequency of 915 MHz. As can be seen, the calculated 10-g averaged SAR values for all scenarios are significantly lower than

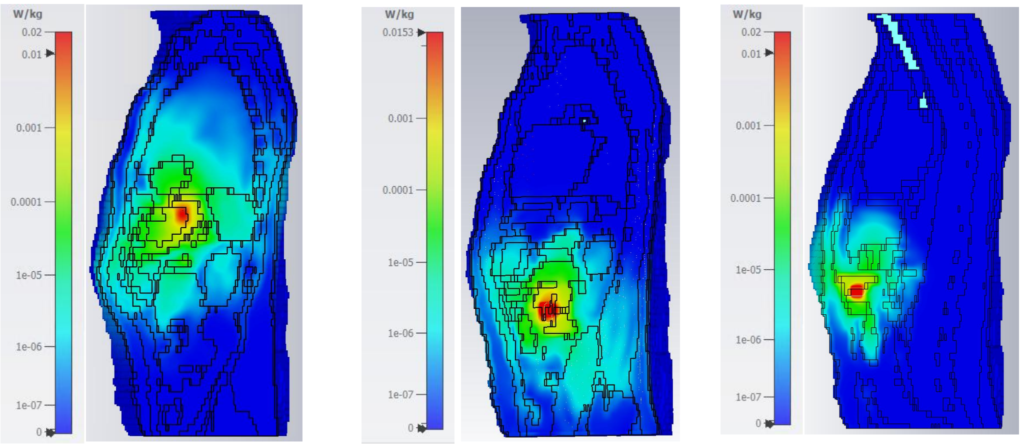

Stomach **Small intestine** **Large intestine**

Figure 4.10: 10-g averaged SAR distribution at 915MHz when antennas are placed in stomach, small intestine, and big intestine.

the 2 W/kg limit specified by the IEEE C95.1-2019 standard. The highest SAR value, 0.0202 W/kg, is observed when both antennas are excited simultaneously, and the capsule is located within the stomach and large intestine. The SAR values for single antenna excitation and small intestine placement are found to be 0.0101 W/kg and 0.0153 W/kg, respectively. These results consistently demonstrate that the proposed antenna system maintains a low level of EM exposure, ensuring patient safety for operation within the GI tract, making it a suitable candidate for WCE applications.

Table 4.1
RELEVANT VARIABLE FOR LM ANALYSIS

Specification	Variable	Value
Operation Frequency (GHz)	f	0.915
Implantable Antenna Gain (dBi)	$\mathrm{G_t}$	-34
Transmitted Power (dBm)	$\mathrm{P_t}$	-16
Transmitter Mismatching Losses (dB)	$\mathrm{L_t}$	0
Distance (m)	d	0-20
Path Loss (dB)	$\mathrm{L_p}$	Distance dependent
Path Loss Exponent	γ	1.5
Shadowing Effect (dB)	$\mathrm{S_e}$	4
Receiving Antenna Gain (dBi)	$\mathrm{G_r}$	2.1
Receiver Mismatching Loss (dB)	$\mathrm{L_r}$	0
Feeding Losses (dB)	$\mathrm{L_f}$	2
Polarization Mismatching Losses (dB)	PL	0.6

4.4.4 Link Margin Analysis

The primary objective of wireless capsule endoscopy is the transmission of photographic and video data from the human digestive to an external receiver. Throughout this period, to maintain the effective transmission of biological data by telemetry equipment to the receiver point, the parameter Link Margin (LM) is important. This parameter assesses the backup signal strength in the wireless communication system, ensuring the maintenance of sufficient signal strength for stable connection. The calculation of LM takes into account free-space loss, polarization-matching loss, path loss, shadowing effects, and feeding loss [44]. To guarantee stable transmission in complex environments, LM must always exceed 0 dB. In this research, the proposed antenna operates as a transmitter, while the receiver is suggested to be a dipole antenna [35]. The polarization loss matching value is considered to be 0.6 dB. Furthermore, to avoid interference with adjacent equipment the transmit power of the implanted antenna is constrained to -16 dBm (25μW). All the parameters required for calculating LM are detailed in Table 4.1.

The mathematical representation of the LM is provided as (5.3).

$$LM = P_a - P_r \tag{4.5}$$

P_a denotes the energy available from the system, while P_r represents the energy requisite for system operation. The expression of P_r can be represented as (5.4)

$$P_r(dB) = \frac{E_b}{N_0} + KT_0 + B_r \tag{4.6}$$

where E_b/N_0 denotes the ratio of bit energy to noise power spectral density which indicates the system's noise tolerance. In this study, this value is set as 9.6 dB. K and T_0 represent the Boltzmann Constant and reference temperature, respectively. The transmission bit rates (B_r) are configured at 1 Mbps, 10 Mbps, 25 Mbps, and 78 Mbps. P_a can be expressed as (5.5)

$$P_a(dB) = P_t + G_t + G_r - PL - L_p \tag{4.7}$$

P_t signifies the transmission power limitation of the implanted antenna, G_t denotes the peak gain of the proposed antenna, G_r represents the gain of the external receiving antenna, PL indicates the polarization mismatching loss and L_p corre-

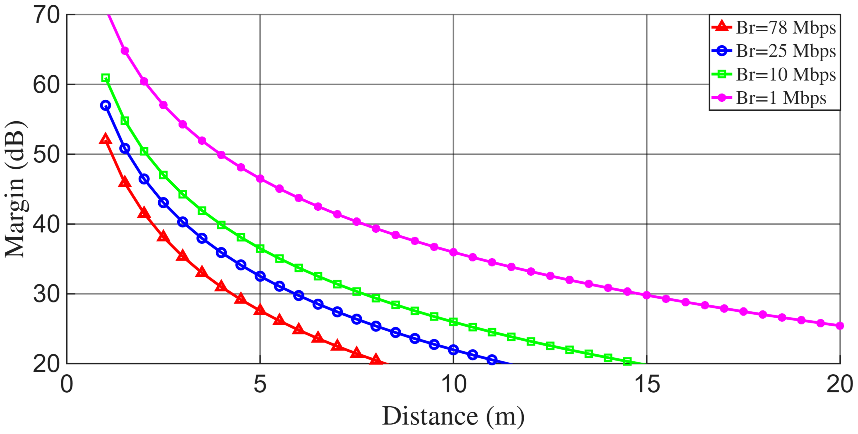

Figure 4.11: The Link Margin of the proposed antenna model at 915 MHz.

sponds to the path loss which can be represented as

$$L_p(dB) = 20\log_{10}(\frac{4\pi d}{\lambda}) + 10\gamma\log_{10}(\frac{d}{d_0}) + S_e \tag{4.8}$$

where d is the distance between transmitter and receiver, γ represents the path-loss exponent, and S_e characterizes the shadowing effect, which describes the impact of obstacles on transmission. As illustrated in Fig. 4.11, effective wireless communication links are tested for distances of 7 m, 4 m, 3 m, and 2 m at data rates of 1 Mbps, 10 Mbps, 25 Mbps, and 78 Mbps, respectively, with more than 20 dB margin. Furthermore, considering the high data rate demands of indoor bio-telemetry applications, a range of 5 - 8 meters may be of particular interest [26].

4.4.5 MIMO Channel Capacity

$$CC = \log_2(det[I + \frac{SNR}{N}HH^*]) \tag{4.9}$$

Compared to SISO antennas, MIMO antennas offer the advantage of enhancing the antenna's channel capacity without extra spectrum resources or increased transmit power. In WCE applications, channel capacity significantly influences the quantity and quality of transmitted images. A high channel capacity enables the transmission of higher resolution images, thus offering a more detailed view. Conversely, the limited channel capacity may cause image compression, potentially distort image quality and impacting diagnosis. Therefore, channel capacity is a critical metric for assessing WCE antennas. The channel capacity of a $N \times N$ MIMO system can be represented as (4.9). In (4.9), CC means channel capacity, N is the number of channels, SNR represents signal-to-noise ratio, I means the identity matrix, H and H* are channel matrix and conjugate of the channel matrix, respectively. As [28] shows, the channel matrix contains the effects of various transmission media, which can be represented as (4.10),

$$H = \sqrt{\Psi_t}G\sqrt{\Psi_r} \tag{4.10}$$

H represents the channel matrix, Ψ_r and Ψ_t are the receive correlation matrix and transmit correlation matrix, respectively. G is a random matrix following Gaussian distribution. The receiving correlation matrix(Ψ_r) and the transmitting correlation matrix(Ψ_t) are directly related to the antenna's radiation pattern. Specifically, these can be articulated as expressed in (4.11).

$$\Psi_{r/t} = \frac{\mu_{ij}}{\sqrt{\mu_{ii}\mu_{jj}}} \tag{4.11}$$

and

$$\mu_{i,j} = \int_0^{2\pi} (XPD \times An_{i,\theta}An^*_{j,\theta} + An_{i,\phi}An^*_{j,\phi})d\phi \tag{4.12}$$

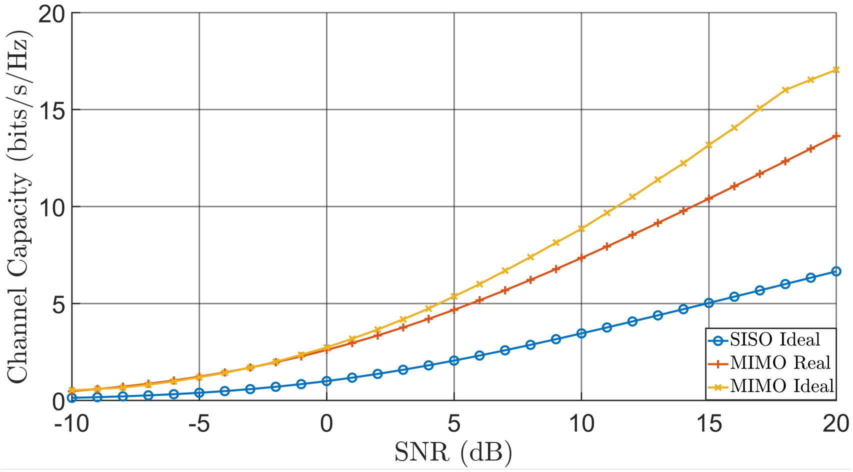

Figure 4.12: The channel capacity of SISO (ideal), MIMO (proposed), MIMO (ideal).

where $\mu_{i,j}$ indicates the channel correlation coefficient, cross polarization discrimination is represented as XPD, and $An_{i,\theta}$, $An_{i,\phi}$ represents the 3D radiation pattern gain of MIMO antennas.

Fig. 4.12 shows the channel capacity based on SISO ideal, MIMO proposed, and MIMO ideal. It is shown that the channel capacity offered by the proposed MIMO antenna model significantly exceeds that of an ideal SISO antenna, yet falls short of an ideal MIMO antenna's capacity, primarily due to the mutual influence between channels. Therefore, the proposed MIMO system can support high-data transmission, such as a high-resolution image or real-time video transmission.

4.4.6 Envelope Correlation Coefficients

In the analysis of MIMO antenna systems, examining the envelope correlation coefficients (ECC) serves as a method for measuring crucial indicators of MIMO systems. This is because ECC effectively captures the correlation between various MIMO channels. In an ideal scenario, the channels of MIMO antennas operate without any interference among themselves, implying an ECC value of 0. However, in practical circumstances, channel interference is inevitable, leading to the conclusion that a lower ECC value is preferable. ECC can be derived from S-parameters and far field radiation patterns gain. The equation for ECC calculation based on S-parameters

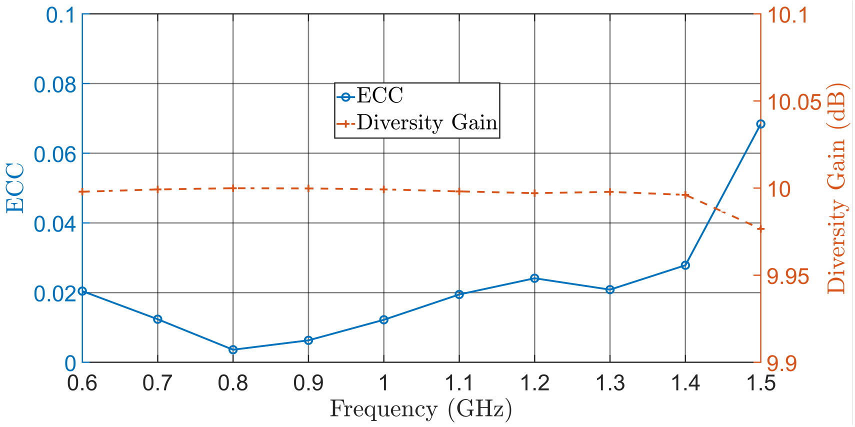

Figure 4.13: The ECC and DG at bandwidth.

is presented as (4.13).

$$ECC = \frac{|S_{11}S_{12}^{*} + S_{21}^{*}S_{22}|}{(1-|S_{11}|^2-|S_{21}|^2)(1-|S_{22}|^2-|S_{12}|^2)} \tag{4.13}$$

In (4.13), S_{11} and S_{22} denote the reflection coefficients of antenna 1 and antenna 2, respectively. S_{12} and S_{21} signify the transmission coefficients from antenna 1 to antenna 2 and vice versa. S_{12}^{*} and S_{21}^{*} represent the conjugates of these two parameters. The radiation pattern based formula shows as (4.14),

$$ECC = \frac{\left|\iint_{4\pi}\left(\vec{An}_i(\theta,\phi)\right)\times\left(\vec{An}_j(\theta,\phi)\right)d\Omega\right|^2}{\iint_{4\pi}\left|\vec{An}_i(\theta,\phi)\right|^2 d\Omega\cdot\iint_{4\pi}\left|\vec{An}_j(\theta,\phi)\right|^2 d\Omega} \tag{4.14}$$

where $\vec{An}_i(\theta,\phi)$ and $\vec{An}_j(\theta,\phi)$ are 3-D radiation pattern of Antenna-1 and Antenna-2 and Ω represents the solid angle. To assess the signal quality and reliability of MIMO antennas, the concept of diversity gain (DG) is utilized to evaluate the enhancement in antenna system performance. The DG can be calculated as (4.15)

$$DG = 10\sqrt{1-(ECC)^2} \tag{4.15}$$

The ECC and DG are presented in Fig. 4.13, Within the antenna's operating frequency range, the acquired ECC value is below 0.1, and the DG value exceeds

Table 4.2
ANTENNA PARAMETERS: COMPARATIVE TABLE WITH THE STATE-OF-THE-ARTS (NM: Not Mentioned)

Reference	[?]	[29]	[7]	[25]	[30]	**This Work**
Frequency (MHz)	2450	2450	433	915	2450	**915**
FBW (%)	13	16	33.9	12.02	8.5	**84.91**
Antenna Size (λ^3)	6.72×10^{-5}	23.94×10^{-5}	27.6×10^{-5}	0.0256×10^{-5}	7.056×10^{-5}	$\mathbf{0.0468 \times 10^{-5}}$
Antenna Structure	Planar	Conformal	Planar	Planar	Planar	**Conformal**
System Type	Capsule	Capsule	Capsule/Implantable	Capsule	Implantable	**Capsule**
Elements	2	2	2	2	2	**2**
Isolation (dB)	28	25	26	29	22	**20**
ECC	< 0.1	NM	< 0.1	< 0.1	NM	**<0.1**
CC@SNR = 20dB(bps/Hz)	9.9	NM	10.2	9.4	NM	**14**

9.9 dB.

A comparative analysis of current research and the proposed work is presented in Table II. Relative to existing work, the model introduced in this study not only boasts a more compact geometric structure but also stands out as the sole design featuring ultra-bandwidth characteristics among MIMO designs. Additionally, compared with other studies, this model exhibits a higher channel capacity due to its ultra-wide bandwidth. Moreover, it can effectively mitigate frequency detuning offered by the heterogeneous GI tract.

4.5 Conclusion

An implantable MIMO antenna for a minimal-sized capsule endoscope has been designed, optimized, simulated, and experimentally validated in this chapter. The proposed MIMO configuration consists of two conformal radiators positioned on the upper and lower sections of the capsule, each fed by an independent port. It exhibits ultra-wideband performance within the designated operating frequency range. By combining multiple folding techniques and meandered structures, the antenna achieves a compact footprint of 30.5 mm × 15 mm × 0.04 mm, corresponding to a volume of 18.3 mm$^{\mathbf{3}}$. In addition, strategically placed holes between the two elements enhance impedance matching and mutual isolation. The final design achieves an FBW of 84.91%, an isolation level of 20 dB, an envelope correlation coefficient (ECC) below 0.1, a diversity gain (DG) exceeding 9.9 dB, and a channel capacity of

14 bps/Hz at an SNR of 20 dB. These results confirm the effectiveness of the proposed conformal MIMO structure in addressing the challenges of frequency detuning and limited channel capacity in WCE applications.

Despite the promising results, several limitations remain. The MIMO structure, while compact, still occupies portions of the capsule's internal wall, leaving limited space for further integration of imaging optics or additional biomedical sensors. Moreover, the metallic surface of the current antenna restricts its placement near the camera aperture, as it obstructs the optical path and degrades image quality. Therefore, to further improve space utilization and enable multi-sensor integration, a transparent antenna solution is required—one that allows electromagnetic radiation and optical transmission to coexist within the same physical aperture.

In the next chapter, a transparency–conductivity mapping model is developed to characterize the electromagnetic performance of conductive transparent materials across a wide frequency range. Based on this model, a transparent UWB antenna design is proposed for capsule endoscopy, aiming to extend the antenna's functionality to the optical domain while maintaining high electrical efficiency and conformal integration.

CHAPTER 5

The Design of Transparency antenna

The previous chapter presented a miniaturized conformal MIMO antenna system for WCE, achieving UWB operation and enhanced channel capacity within the highly constrained capsule volume. While this design effectively improves spatial utilization and electromagnetic performance, the metallic nature of conventional antennas inevitably obstructs the optical path when placed in close proximity to the imaging module. This limitation prevents the effective use of the capsule dome, a region that is otherwise highly attractive for antenna integration due to its proximity to the camera and its potential to further alleviate internal space constraints. To overcome this challenge, transparent antenna technology is introduced in this chapter, enabling simultaneous electromagnetic radiation and optical transmission. By employing radiating structures with high optical transmittance and sufficient electrical conductivity, antennas can be positioned directly over the camera aperture, thereby improving overall system compactness and facilitating the integration of additional sensing modules or increased battery capacity. Although transparent antennas have been investigated in various applications such as wearable electronics, vehicular systems, and display-integrated platforms, their application in wireless capsule endoscopy remains largely unexplored. The stringent requirements of WCE—including extreme size constraints, curved integration surfaces, in-body electromagnetic loading, and strict biocompatibility considerations—pose unique challenges that are not adequately addressed by conventional transparent antenna designs. Therefore, before introducing the proposed transparent antenna solution, it is necessary to review existing transparent antenna technologies and assess their suitability for capsule-based biomedical applications. This section first summarizes the state of the art in transparent antenna design, followed by a discussion of their limitations in the context of WCE, which motivates the development of a conductivity–transparency mapping model and the inkjet-printed transparent antenna presented in this chapter.

5.1 Introduction and Background

Currently, antennas for WCE are mainly constructed using rigid substrates [38, 45] placed between multiple electronic components within the capsule or flexible materials [20, 46] attached to the capsule's inner walls. However, the dome area of the capsule remains underutilized. By relocating antennas to the capsule dome, more internal space could be freed for additional detection equipment, thereby expanding functionality, or for increased battery capacity to extend operation time. Nevertheless, traditional opaque antennas placed in this area would significantly block the optical performance of the camera. Hence, transparent antenna technology is introduced to address this problem. Transparent antennas positioned in the capsule dome effectively utilize limited internal space and maintain unobstructed visibility for the embedded camera.

Currently, there are two primary technical approaches to achieving antenna transparency. One such approach involves designing the antenna with a conductive film that exhibits high optical transmittance. Among these materials, transparent conducting oxides (TCOs) are the most widely used transparent conductors. Among the common TCOs compounds, the antennas based on the material indium-tin-oxide (ITO) were present [47]. The author developed a monopole antenna with -1.96 dBi gain and over 80% transparency. Similarly, a circular patch antenna designed based on the material fluorine-doped tin oxide (FTO) achieved 3.63 dBi gain and 74.29% transparency [48]. Despite, TCOs materials have excellent transparency and electromagnetic properties, they are highly limited in mechanical stress applications due to their inherent brittleness. In addition, the fabrication and processing of this material require advanced techniques, such as RF sputtering, which operates exclusively in vacuum environments and at high temperatures. This process not only demands precise control of deposition parameters but also significantly increases production costs, thereby hindering large-scale manufacturing.

Another approach involves using a metal mesh(MM) structure to achieve a balance between electromagnetic characteristics and transparency.This approach enables a trade-off between transparency and conductivity by adjusting the mesh structure and size. In [49], The authors propose a patch antenna with a rectangular metal grid on a glass substrate to enhance transparency. The antenna ultimately achieves a gain of 11.9 dBi while maintaining 70% transparency. In addition to this, a transparent antenna with UWB and MIMO characteristics is proposed in [50]. The authors also chose to dig holes in the surface of the antenna to achieve optical transparency and used CPW excitation to please the effect of the dielectric plate on the transparency. Finally, the design achieves a gain of 3.0 dBi at 77% transparency. In addition, polyethylene terephthalate(PET) is used as a flexible, optically transparent medium in [51] for the fabrication of transparent antennas. The authors employ a circular patch antenna structure and a metamaterial (MM) to achieve antenna transparency. The design ultimately achieves a bandwidth of approximately 200 MHz and a transparency of 64%. However, It is worth to note that the overall size of the antennas studied in [49–51] is significantly large, limiting their applicability in the medical and healthcare field. Additionally, these designs are primarily fabricated using metal etching and laser cutting, leading to longer production cycles for large-scale manufacturing and design iterations.

Inkjet printing technology, which utilizes conductive inks for conductor fabrication, presents a more attractive solution. This technology enables precise control over pattern geometry, material deposition, and manufacturing costs, facilitating rapid production and iterative design improvements [52]. While inkjet printing technology has been explored for transparent conductor [53], these studies have mainly focused on a fixed transparency, so there is a research gap based on the correlation between optical and electromagnetic properties. The mapping relationships in these properties are crucial for optimizing transparent antennas.

This study investigates the effect of mesh structures on optical and electromagnetic properties using nano-silver conductive inks and inkjet printing techniques. Mapping relationships are modeled based on rectangular patterns and transmission lines to establish the correlation between transparency, conductivity, and mesh size. Utilizing these mapping model, a compact transparent antenna with ultra-wide bandwidth is proposed for capsule endoscopy. To the best of the author's knowledge, this work represents the first implementation of transparent antenna technology in the context of WCE, providing a new pathway toward optically compatible and space-efficient implantable antenna design.

5.2 Conductivity and Transparency Mapping Model

5.2.1 Materials and Equipment

The conductive material used is Metalon® JS-A291 silver nanoparticle ink (Novacentrix), selected for its high conductivity and compatibility with the inkjet printing process. According to the manufacturer's data sheet, the ink achieve a volume resistivity of $3.7\times10^{-4}\,\Omega\cdot\text{cm}$ when thermally cured at 175°C for 10 minutes. Glasses with a thickness of 2 mm are used for printing, providing reliable mechanical stability while ensuring sufficient optical transparency and compatibility with RF characteristics. The manufacturing process mainly utilizes Fujifilm Dimatrix DMP-2850 inkjet printers. This printer offers a maximum resolution of 5080 dpi. Electromagnetic characteristics were measured and analyzed using a Tektronix TTR506A Vector Network Analyzer (VNA), which operates in the frequency range of 300 KHz to 6 GHz. To ensure a reliable electrical connection between the SMA connector and the printed conductor, RS PRO Liquid Adhensive (Conductive Epoxy) was applied. Subsequently, the connection was cured at 100°C for 20 minutes to ensure proper fixation. The ground plane was formed using copper tape adhered to the bottom

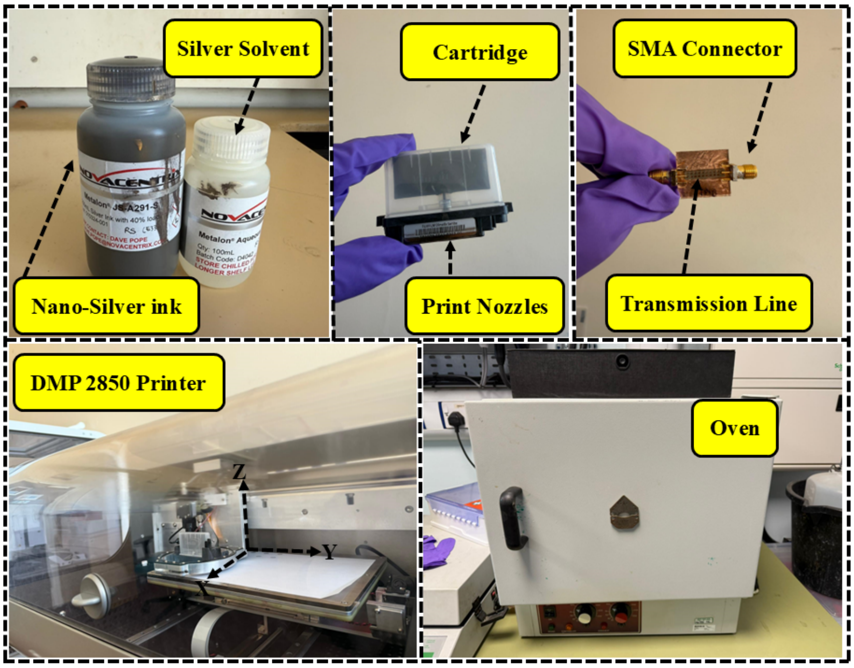

Figure 5.1: Equipment and materials required for the fabrication of transmission lines.

surface of the glass substrate, providing a stable reference for signal propagation. All the equipment and material are presented in Fig. 5.1.

5.2.2 Design of Transparency Conductive Mesh Pattern

To evaluate the frequency-dependent conductivity of the conductive ink, a 50-ohm transmission line was designed and printed on a glass substrate, as Fig. 5.2. The optical transparency of the printed transmission line is controlled by a rectangular grid design, as illustrated in Fig. 5.3. Ten rectangular mesh meshes are evenly spaced in the top and bottom rows of the transmission line, and the mesh structure consists of line width(W) and length(L) as well as the periodicity of the mesh edge length(I). The theoretical transparency(T) can be expressed as:

$$T = \frac{20I^2}{WL} \tag{5.1}$$

Five transparency levels - 90%, 80%, 70%, 60%, and 50% - were achieved by adjusting the mesh edge I to 1.36 mm, 1.28 mm, 1.2 mm, 1.11 mm, and 1.01 mm, respectively, while keeping the overall L and W of the transmission line constant.

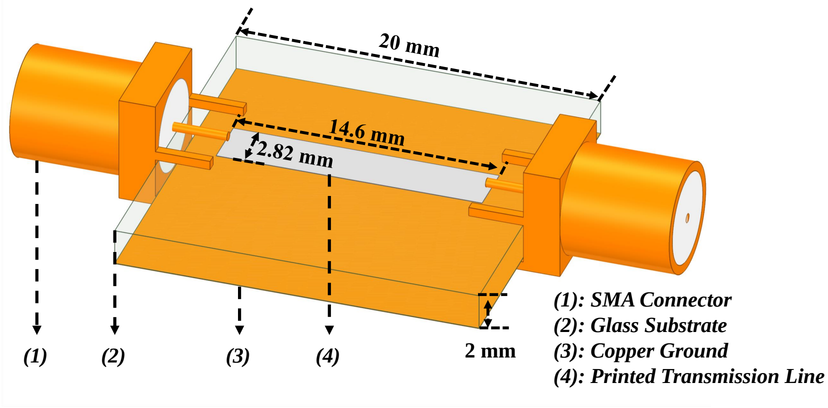

Figure 5.2: Transmission line model.

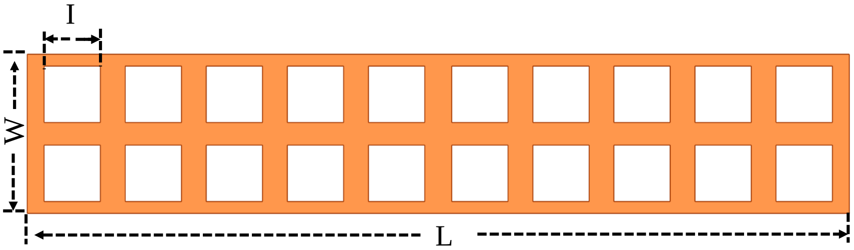

Figure 5.3: Transparency mesh pattern.

5.2.3 Fabrication and Characterization of Mesh-Based Transparent Conductive Films

The thickness of mesh-based conductive films significantly influences electrical properties of transparent transmission lines. To determine the optimal number of printed layers, the characterization process described above was first applied to opaque transmission lines with different printed layer counts. The conductivity values extracted from these reference metrics help to create the minimum thickness required for effective RF performance, which is then realized in the fabrication of the transparent line.

Multiple printing layers were deposited using DMP-2850 printer. Five minutes of natural air drying is allowed between each layer of printing to ensure the stability of each layer. And then placed at 175°C for ten minutes to thermal curing. Samples with different number of layers and transparency are manufactured in multiples to ensure reliability. The S_{12} measurement range of all samples is guaranteed to be

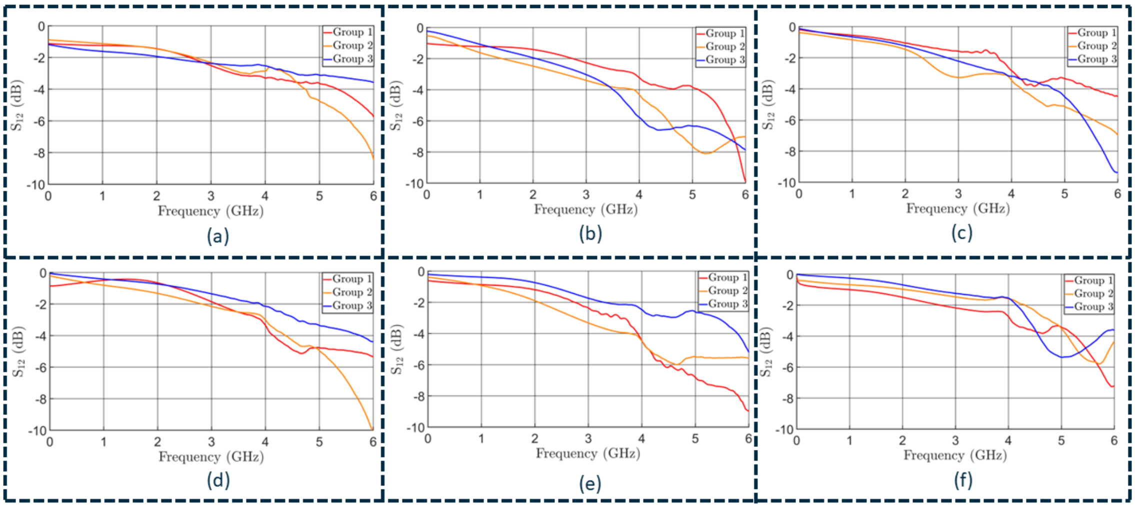

(a) (b) (c) (d) (e) (f)

Figure 5.4: Measured S_{12} of transmission line with (a)-(f) One to six layers.

between 1 and 6 GHz. Average the S_{12} parameters measured in multiple samples with each transparency to obtain representative transmission characteristics. Then, to determine the effect of transparency variations on the frequency-dependent conductivity of silver conductive ink printed films, electromagnetic simulation software Ansys HFSS was employed to construct simulation models identical to the experimental samples, setting various conductivity conditions to obtain corresponding simulated S12 data. Finally, the experimentally averaged S_{12} data was compared with the simulated data at each frequency point to identify the most closely matched the measured response. This result was identified as the estimated frequency based conductivity. This process was repeated over the entire frequency range to create a frequency-dependent conductivity profile of the transparent conductive film.

5.2.4 Optimization of printed layer thickness

The electromagnetic characteristics of inkjet-printed transmission lines can be influenced by various factors, among which the skin effect is particularly significant. At high frequencies, the skin effect causes current to concentrate near the surface of the conductor, resulting in a decreasing penetration depth. This reduces the effective conductor area and consequently increases signal losses. Therefore, the optimal printing thickness was determined by fabricating samples with multiple printed layers. To explore the complex relationship between thickness and RF performance of

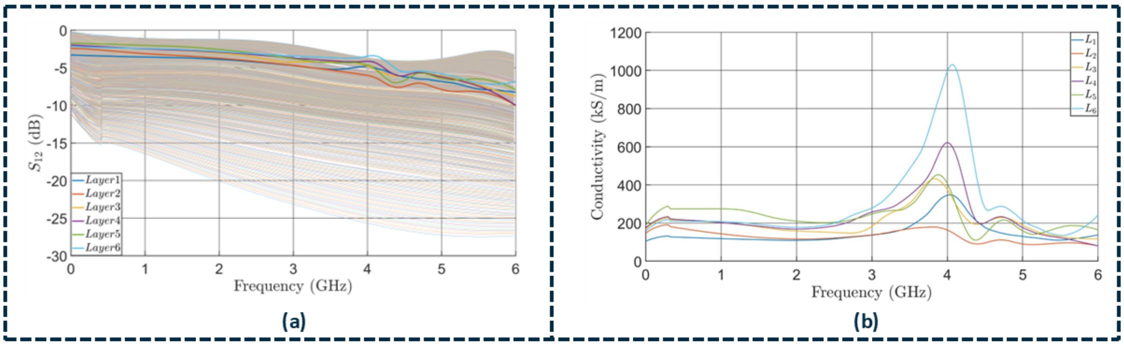

Figure 5.5: (a)Averaged S_{12} for printed transmission line with multiple layers. (b) Extracted conductivity based on frequency.

printed transmission line layers, samples with varying layer counts were fabricated, with three replicas produced for each configuration. Fig. 5.4(a) - (f) present the measured S_{12} of printed transmission line for multiple layers. Fig. 5.5(a) presents the averaged S_{12} comparing with simulation to extract the conductivity. It is clearly observed that the measured S_{12} parameter increases with the number of printed layers. Conductivity based on frequency variation is demonstrated in Fig. 5.5(b). Contrary to the expected outcome based on the skin effect, the extracted frequency-dependent conductivities do not exhibit a monotonically decreasing trend but instead demonstrate a highly complex frequency dependence. This phenomenon may result from the unique structural characteristics of silver nanoparticles. Due to the inability of inkjet printing to produce a perfectly uniform distribution of nanoparticles, the conduction mechanisms at particle interfaces and interlayer boundaries differ significantly from those in bulk metals. Additionally, the effective conductivity reflects the combined influence of material properties, print geometry, and various frequency-dependent loss mechanisms. Notably, as conductivity increases with the number of printed layers, the edge effect becomes more pronounced by the fifth layer. This indicates that five-layer printing achieves an optimal balance between fabrication complexity and RF performance. This criterion was subsequently used to guide the development of transparent constitutive configurations.

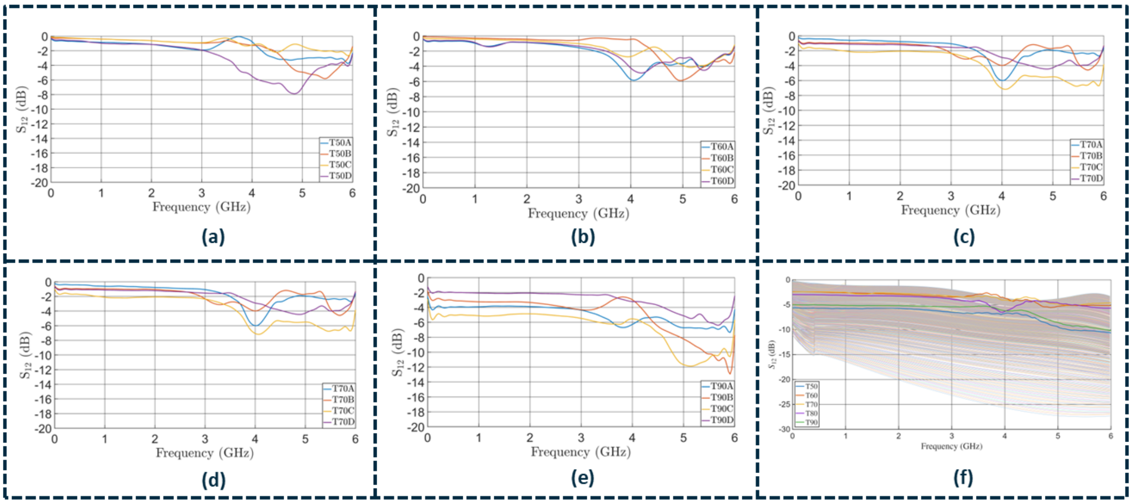

Figure 5.6: (a) - (e) Averaged S_{12} for printed transmission line with different transparency. (f) Extracted transparency-conductivity based on frequency.

5.2.5 Performance of Mesh-Based Transparent Conductivity Films

Building on the previously optimized five-layer prints, transparent transmission lines with varying grid sizes were fabricated. Four samples were produced for each transparency level to evaluate consistency and reliability. Fig. 5.6(a) to (e) demonstrate the S_{12} measurement for samples with 50%, 60%, 70%, 80%, and 90% transparency respectively. Notely, when the transparency of the sample increases, the S_{12} value decreases significantly due to the reduced current path strength in the transparent configuration. Furthermore, the measurement differences between samples increase significantly with rising transparency, particularly in samples with 90% transparency. Additionally, as the mesh becomes sparser, small variations in line width or continuity have proportionally greater impacts on performance. This effect is particularly pronounced at high frequencies, indicating that the relationship between mesh geometry and conductivity becomes increasingly complex as the wavelength decreases. The average S_{12} results across all transparency levels are presented in Fig. 5.6(f), providing a clear visualization of the trade-offs in transparency performance. Fig. 5.7 presents the extracted effective conductivity values for different transparency levels. The grid structure significantly alters the current distribution compared to a solid conductor, resulting in an effective conductivity that reflects both material

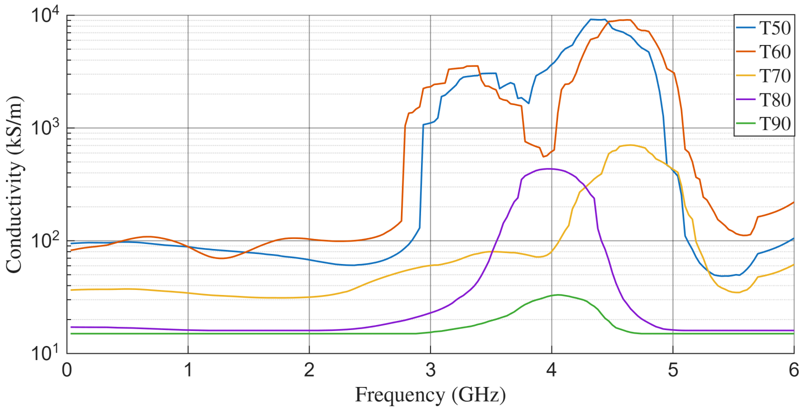

Figure 5.7: The varying conductivity with different frequency

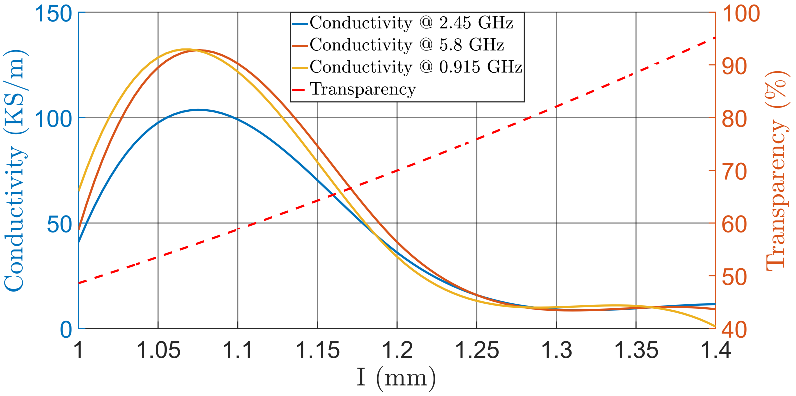

Figure 5.8: Comparison of conductivity at 915 MHz, 2.4 GHz, and 5.8 GHz under varying transparency

properties and geometrical effects. To support practical design decisions, Fig. 5.8 presents a novel mapping of electrical performance, optical transparency, and mesh geometry parameters. The figure is constructed using the 915 MHz, 2.4 GHz, and 5.8 GHz ISM bands; however, similar mappings can be generated for any frequency within the characteristic range to meet specific application requirements. This visualization enables designers to directly identify the grid configuration that satisfies the desired combination of electrical and optical properties. For instance, achieving 70% transparency while maintaining conductivity above a defined threshold requires specific grid size ratios, which are clearly identifiable from the mapping.

5.2.6 Long-term Degradation Considerations for Transparent Antennas

The RF performance of transparent antennas is ultimately governed by the effective conductivity of the transparent conductor. For inkjet-printed silver mesh structures, the conductivity (or equivalently the sheet resistance) may degrade over time (e.g., over a one-year timescale) due to chemical, environmental, and mechanical factors. This potential drift should be considered together with the transparency–conductivity trade-off, since any increase in resistive loss can directly reduce radiation efficiency and realised gain, and may also perturb the resonance condition.

From a materials perspective, degradation may arise from oxidation/sulfidation of silver, moisture ingress that weakens inter-particle electrical connectivity, micro-cracking and partial delamination induced by handling or bending, and changes at the conductor–substrate interface. All these mechanisms effectively increase conductor resistance, leading to higher ohmic loss. In antenna terms, reduced conductivity results in lower radiation efficiency (and thus lower realised gain), while the altered current distribution can cause resonance drift and degraded impedance matching. Therefore, transparent antennas with very high optical transmittance (i.e., low conductive coverage) are generally more sensitive to further conductivity reduction, because their initial "conductivity headroom" is limited.

To quantify the expected impact of one-year aging without requiring year-long waiting, a sensitivity analysis can be performed using the conductivity–frequency model established in this chapter. The aged conductivity can be parameterised as

$$\sigma_{\text{aged}}(f) = \eta\, \sigma_{\text{initial}}(f), \quad 0 < \eta \leq 1, \tag{5.2}$$

where $\sigma_{\text{initial}}(f)$ is the initially extracted effective conductivity and η represents an aging factor. Representative cases such as $\eta = 0.8$, 0.6, and 0.5 (corresponding to 20%, 40%, and 50% conductivity reduction) can be evaluated to observe the resulting changes in $|S_{11}|$, realised gain, and total radiation efficiency (and axial ratio where circular polarisation is required). For the proposed transparent prototype with $\sim$ 70% measured optical transparency operating over 2–3 GHz, this analysis provides a direct link between plausible conductivity degradation and expected RF performance drift. In general, a reduction in conductivity is expected to increase conductor loss and reduce radiation efficiency; consequently, the transparency level should be selected not only to meet optical requirements but also to maintain sufficient conductivity margin over the intended lifetime.

In terms of practical mitigation, thin encapsulation layers (dielectric overcoats), improved curing/sintering conditions, and mesh-geometry optimisation (e.g., avoiding overly narrow traces that are prone to cracking) can improve stability. Experimental verification can be performed via accelerated aging tests (e.g., elevated temperature/humidity exposure and repeated bending cycles) followed by periodic measurements of sheet resistance and antenna metrics. These steps help ensure that the transparent antenna remains within the required performance envelope over time while preserving the intended optical transmittance.

5.3 Implantable Antenna Design Methodology

Based on the transparency–conductivity mapping model developed in the previous section, the conductivity data corresponding to 70% transparency is used to design the transparent antenna in the subsequent stage. The configuration of the proposed WCE is depicted in Fig 5.9(a). Along the horizontal direction from left to right are the transparent capsule lid, the antenna assembly, the camera or optical sensor, the battery with the battery holder, and the printed circuit board(PCB) and PCB holder. All components are encapsulated in a 3D-printed, biocompatible polyimide ($\varepsilon_r = 3.5$, $\tan\theta = 0.008$) capsule shell. The detailed geometric parameters of the antenna are demonstrated in Fig. 5.9(b). Since inkjet printing is employed in the fabrication process, a coplanar waveguide is used to excite the antenna. For ease of visualization, the model excludes the mesh structure. Fig. 5.9(c) displays the proposed WCE model from various viewing angles. The antenna's substrate is composed of silica glass with a diameter of 10 mm and a thickness of 2 mm, offering stable electromagnetic performance and high transparency.

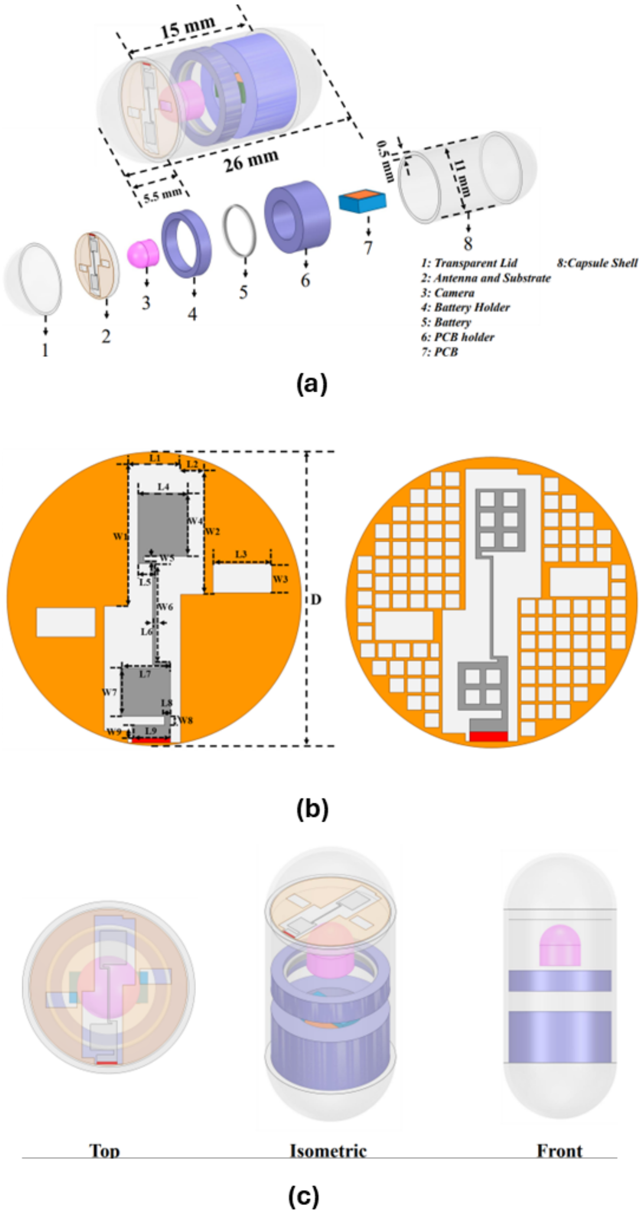

Figure 5.9: (a) The elements configuration of proposed WCE. (b) Simulation model(left) and transparent antenna top view(right). (c) Top, isometric, and front view of WCE model. The geometrical dimension of planar antenna: $L_1 = 1.8$, $L_2 = 0.8$, $L_3 = 2$, $L_4 = 1.7$, $L_5 = 0.5$, $L_6 = 0.1$, $L_7 = 1.7$, $L_8 = 0.2$, $L_9 = 1.3$, $W_1 = 4.85$, $W_2 = 4.25$, $W_3 = 1$, $W_4 = 2.15$, $W_5 = 0.15$, $W_6 = 3.45$, $W_7 = 1.65$, $W_8 = 0.3$, $W_9 = 0.45$, $D = 10$ (Unit: mm).

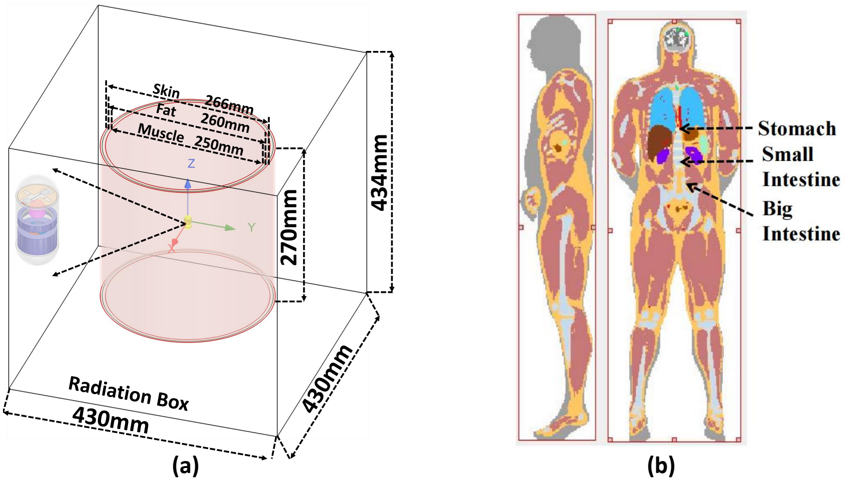

Figure 5.10: Setup of WCE model simulation. (a) Three-layered cylinder phantom model simulation. (b) Heterogeneous human model simulation.

5.3.1 Simulation Environment

The proposed WCE model is initially placed in a phantom model for design purposes and later optimized within a homogeneous model, which is detailed in Fig. 5.11. The battery and PCB are modeled using perfect semiconductor and copper materials, respectively, while polyimide is used for their holders. The camera is modeled with silicon. Initially, the proposed WCE model was placed in a three-layer human tissue cylinder model. The model was built in High Frequency Simulation Software (HFSS). The cylindrical human tissue model comprises muscle, fat, and skin layers arranged from the inside out, presented in Fig. 5.11(a). The dielectric constant and dissipation factor of these tissues vary with frequency [22]. After the preliminary antenna design is completed, the proposed model is placed in a homogeneous human model for optimization. The simulation is conducted using CST Studio Suite. The proposed model is simulated at different regions of GI tract as Fig. 5.11(b).

5.3.2 Evolution Steps

In this study, the proposed antenna model went through four design iterations. Fig. 5.5(a) illustrates the antenna's iterative development process, while Fig. 5.5(b) presents the S-parameters resulting from each iteration. Firstly, considering the typical capsule size for ease of swallowing or implantation, the antenna adopts a circular structure with a diameter of 10 mm. Additionally, since inkjet printing is used to fabricate the antenna, a coplanar waveguide (CPW) is employed for excitation. In step one, a vertical rectangular slot is etched at the center of the antenna to extend the current path and centralize the electric field distribution, thereby enabling effective resonance within a compact form factor. A metal patch is embedded in the center of the slot, serving both to adjust impedance matching and to act as the primary radiating element, providing a foundation for further performance optimization. However, due to the short current path length, the antenna fails to achieve effective resonance within the target frequency band, resulting in an overall reflection coefficient (S_{11}) of approximately -2dB, which indicates poor impedance matching. In the second step, two staggered rectangular slots are introduced into the ground plane on both sides of the central slot. This asymmetrical defected ground structure (DGS) directs current along and around the edges of the rectangular slots, thereby increasing the effective current path length and reducing the resonant frequency. Simulation results show that the S_{11} parameter of the antenna decreases from approximately -2 dB to -5 dB following the introduction of the defected ground structure (DGS), indicating improved impedance matching. However, the response curves do not exhibit a clear resonance, suggesting that the structure alone is insufficient to excite effective modes. Further optimization of the current path and structural coupling is therefore necessary. In the third step, to further improve the antenna's impedance matching, the central metal structure is optimized using a meandered path design. This configuration extends the effective current path length and adjusts impedance without increasing the antenna's overall size. Specifically, wider sections at the top and bottom provide low impedance, while the narrower middle segment introduces high impedance. Impedance matching is achieved by adjusting the position and dimensions of these segments. As a result, the antenna's resonance performance is significantly enhanced by bending and optimizing the dimensions of the central bar structure, extending the effective bandwidth range (S_{11} <-10 dB) from 2.0 GHz to 2.6 GHz, with a minimum value of approximately -16 dB. However, the resonance peak at 2.45 GHz does not fully align with the center frequencies of the ISM bands. Therefore, to precisely position

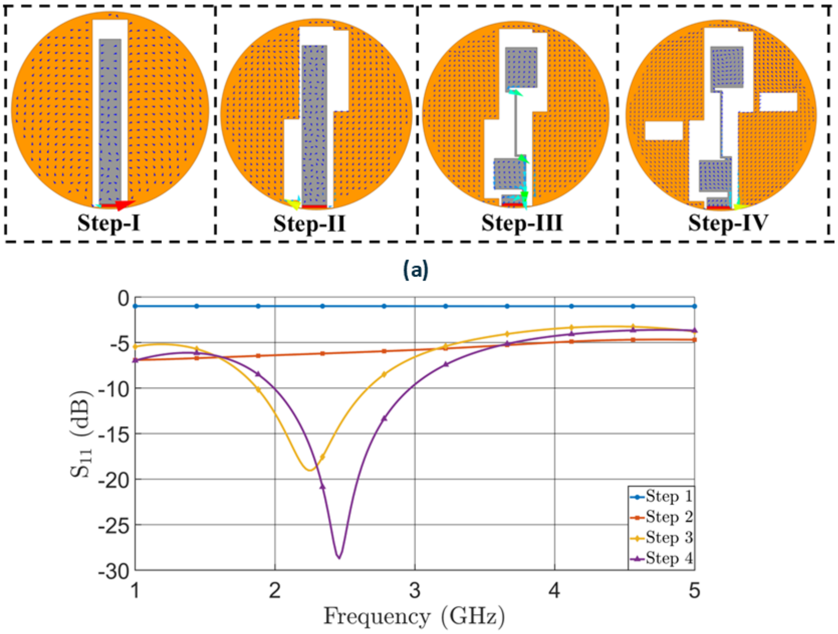

(a)

(b)

Figure 5.11: (a) Evolution steps for antenna. (b) The S-parameter for different antenna evolution.

the resonance frequency, a new structural optimization scheme is introduced in Step 4. In Step 4, two symmetrical rectangular slots are etched into the ground plane on both sides of the antenna to further broaden the bandwidth and precisely align the resonance frequency with the target 2.45 GHz. This structure introduces additional inductive and capacitive elements via ground perturbation, thereby refining the antenna's input impedance and resonance characteristics. Simultaneously, it increases the current path length in the ground plane to enhance electromagnetic coupling between the antenna and the ground. The final simulation results demonstrate that the Step 4 structure significantly enhances antenna performance, extending the effective bandwidth range (S_{11} <-10 dB) from 2.0 GHz to 3.0 GHz with fractional bandwidth 40%. This range not only covers the target frequency of 2.45 GHz but also exhibits excellent ultra-wideband characteristics.

5.4 Results and Analysis

The proposed antenna design is fabricated using the glass substrate (SiO_2) to validate the simulated results. Fabricated antennas prototype are shown in Fig. 5.12(a).

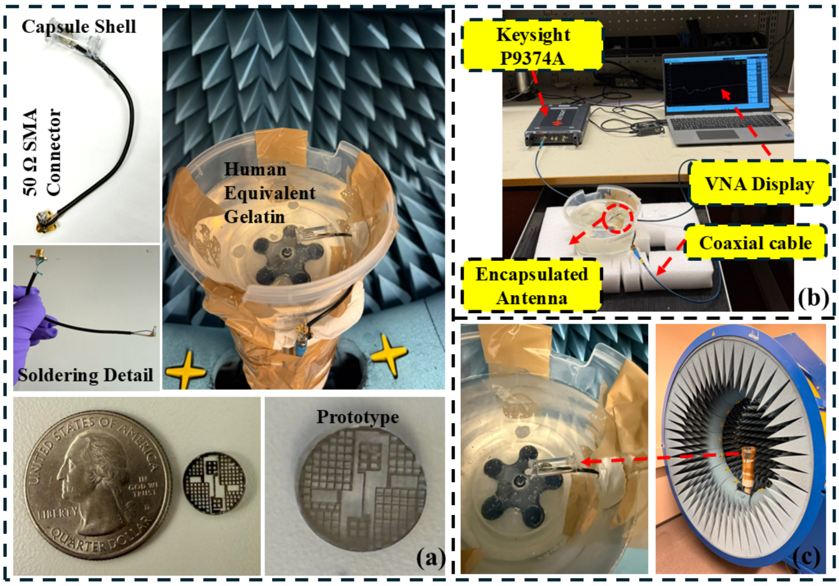

Figure 5.12: (a) The fabricated antenna prototype before and after encapsulating. (b) Setup for Measuring S-Parameters. (c) Setup for Measuring Radiation Pattern

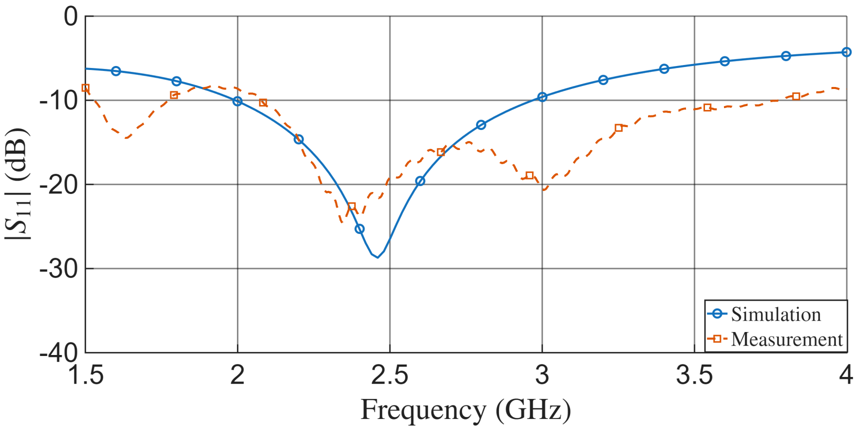

Figure 5.13: Comparison of simulated and measured S-parameters.

For the antenna's S-parameter and radiation pattern measurements, the entire assembly is then immersed in human equivalent Gelatin , serving as a tissue-equivalent material for the human digestive system, as Fig. 5.12(b) and (c).

5.4.1 S-Parameters

The proposed antenna's S-parameters are measured using a Keysight P9374A portable Vector Network Analyzer (VNA), with the antenna elements connected via coaxial cables. The simulated and measured reflection coefficients of the proposed transparent antenna are shown in Fig. 5.13, both the simulated and measured results exhibit UWB impedance characteristics. The simulated $|S_{11}|$ shows a strong resonance at 2.45 GHz, covering a –10 dB impedance bandwidth of 2.0–3.0 GHz (40%). The measured result demonstrates two distinct resonant frequency at 2.4 GHz and 3.0 GHz, with a wider –10 dB bandwidth of 2.1–3.5 GHz ($\approx$50%). The minor discrepancies between the two can be attributed to fabrication tolerances introduced during the inkjet-printing process. In particular, non-uniform deposition of the silver nanoparticle ink may lead to slight variations in the printed layer thickness and surface conductivity, causing small deviations in the measured gain and radiation symmetry.

Overall, the measured data confirm that the fabricated transparent antenna maintains stable and consistent ultra-wideband performance, validating the accuracy of the simulation and the robustness of the proposed design.

5.4.2 Radiation Pattern and Gain

To evaluate the antenna radiation performance in a realistic propagation environment, the fabricated prototype was measured in an anechoic chamber while immersed in a human-equivalent gelatin phantom, as shown in Fig. 5.12(b). During the measurement, one port of the antenna was connected to a spectrum analyzer, and the other port was terminated with a 50 Ω load to prevent signal reflection. A standard high-gain horn antenna was employed as the transmitting source, placed at a distance of one meter from the prototype. The received power was recorded

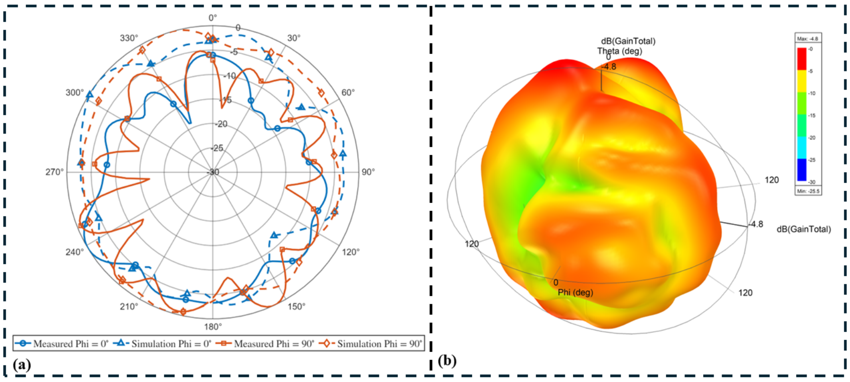

Figure 5.14: (a) Comparison of simulation and measurement radiation pattern at 2.4 GHz. (b) 3D radiation pattern for antenna.

with an angular resolution of 1°, enabling precise reconstruction of the radiation pattern.

Fig. 5.14(a) presents the simulated and measured radiation patterns of the proposed transparent antenna at 2.4 GHz in two principal planes ($\phi = 0°$ and $\phi = 90°$) with 3D radaition pattern in Fig. 5.14(b). The measurement results show good agreement with the simulation, confirming consistent radiation characteristics across both planes.

The simulated radiation pattern exhibits a peak gain of -4.6 dBi, while the measured peak gain is -4.3 dBi. This discrepancy can be attributed to the factors discussed earlier. Despite these differences, both results demonstrate a quasi-omnidirectional pattern, which is advantageous for WCE applications to maintain reliable communication regardless of capsule orientation. As shown in Fig. 5.14(b), the 3D radiation pattern reveals an almost omnidirectional distribution, with strong radiation observed along the upper dome region ($\theta \approx 0°$) and around the azimuthal plane ($\phi = 0°$–$360°$). These regions correspond to the outer ring and top of the capsule, where the gain reaches its maximum value of approximately -4.8 dBi. Such radiation behavior is highly beneficial for WCE applications, as the capsule rotates freely within the GI tract. The enhanced radiation coverage along both the peripheral and top regions strengthens the wireless communication link, maintaining high link reliability and consistent transmission quality even as the capsule changes orientation inside the body.

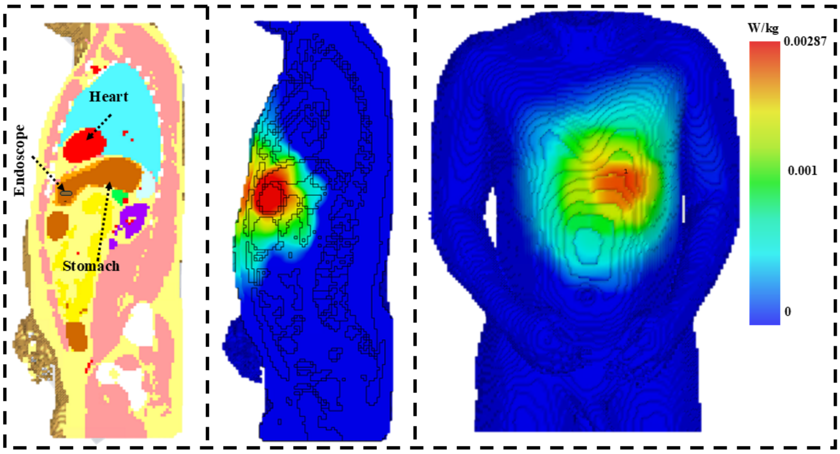

Figure 5.15: 10-g averaged SAR distribution at 2.45 GHz in heterogeneous model.

5.4.3 SAR Evaluation

In WCE systems, the antenna functions inside the human body, making it essential to verify that the electromagnetic (EM) radiation exposure complies with established biomedical safety standards. The specific absorption rate (SAR) quantifies the rate at which EM energy is absorbed per unit mass of tissue, and according to the IEEE C95.1-2019 guideline, the 10-gram averaged SAR should not exceed 2 W/kg [37]. To evaluate the safety of the proposed transparent antenna, full-wave simulations were conducted using a human body model with an input power of 25 μW, following ITU-R RS.1346 recommendations [25]. The capsule was virtually placed inside the stomach to represent its operating environment, as shown in Fig. 5.15. The absorbed power is mainly concentrated near the capsule, with the maximum 10 g-averaged SAR value of 0.00287 W/kg, far below the 2 W/kg safety threshold. This confirms that the proposed antenna operates safely within regulatory limits, providing reliable radiation performance for in-body communication without posing risk to surrounding biological tissues.

5.4.4 Link Margin Analysis

To ensure reliable wireless communication in capsule endoscopy, it is essential to evaluate the link margin(LM) between the implanted antenna and the external receiver. The link margin quantifies how much the received signal exceeds the minimum required threshold, taking into account factors such as path loss, tissue absorption, antenna gain, and system noise. A sufficient link margin ensures robust data transmission, even under varying in-body conditions. The primary factors involved in the evaluation of LM include free-space loss, polarization mismatch loss, path loss, shadowing effects, and feeding loss [26]. To ensure stable and seamless transmission, the LM should be maintained above 20 dB. In this research, the proposed antenna operates as a transmitter, while the receiver is suggested to be a dipole antenna [**?**]. The polarization loss matching value is considered to be 0.6 dB. Furthermore, the transmitted power is limited to -16 dBm (25μW), in accordance with regulatory limits for implantable electronic devices. All the parameters required for calculating LM are detailed in Table II.

The mathematical representation of the LM is provided as (5.3).

$$LM = P_a - P_r \tag{5.3}$$

P_a denotes the energy available from the system, while P_r represents the energy requisite for system operation. The expression of P_r can be represented as (5.4)

$$P_r(dB) = \frac{E_b}{N_0} + KT_0 + B_r \tag{5.4}$$

where E_b/N_0 denotes the ratio of bit energy to noise power spectral density which indicates the system's noise tolerance. In this study, this value is set as 9.6 dB. K and T_0 represent the Boltzmann Constant and reference temperature, respectively. The transmission bit rates (B_r) are configured at 1 Mbps, 10 Mbps, 25 Mbps, and 78 Mbps. P_a can be expressed as (5.5)

$$P_a(dB) = P_t + G_t + G_r - PL - L_p \tag{5.5}$$

P_t represents the transmitted power limit of the implanted antenna, G_t denotes the peak gain of the proposed antenna, G_r represents the gain of the external receiving antenna, PL indicates the polarization mismatching loss and L_p corresponds to

Table 5.1
LM ANALYSIS PARAMETERS

Specification	Variable	Value
Operation Frequency (GHz)	f	2.45
Implantable Antenna Gain (dBi)	$\mathrm{G_t}$	-4.3
Transmitted Power (dBm)	$\mathrm{P_t}$	-16
Transmitter Mismatching Losses (dB)	$\mathrm{L_t}$	0
Distance (m)	d	0-20
Path Loss (dB)	$\mathrm{L_p}$	Distance dependent
Path Loss Exponent	γ	1.5
Shadowing Effect (dB)	$\mathrm{S_e}$	4
Receiving Antenna Gain (dBi)	$\mathrm{G_r}$	2.1
Receiver Mismatching Loss (dB)	$\mathrm{L_r}$	0
Feeding Losses (dB)	$\mathrm{L_f}$	2
Polarization Mismatching Losses (dB)	PL	0.6

the path loss which can be represented as

$$L_p(dB) = 20\log_{10}(\frac{4\pi d}{\lambda}) + 10\gamma\log_{10}(\frac{d}{d_0}) + S_e \tag{5.6}$$

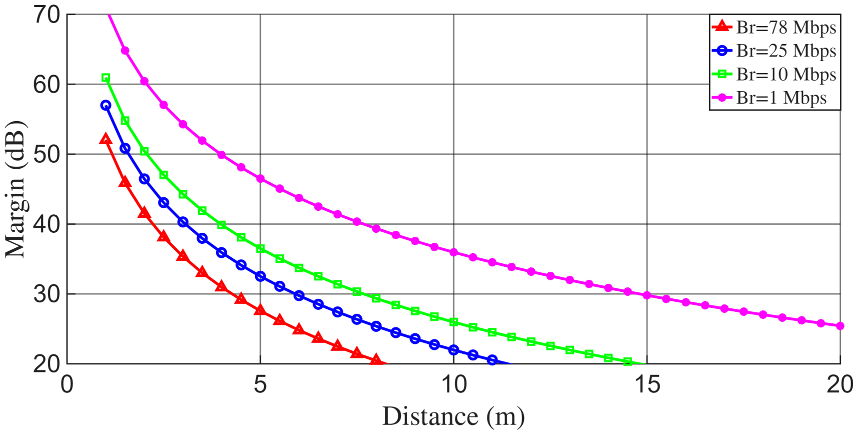

Figure 5.16: The Link Margin of the proposed antenna model at 2.4 GHz.

Table 5.2
ANTENNA PARAMETERS: COMPARATIVE TABLE WITH THE STATE-OF-THE-ARTS

Reference	[35]	[29]	[36]	[45]	[54]	**This Work**
Frequency (MHz)	2450	2450	433	915	2450	**2450**
FBW (%)	13	16	33.9	12.02	8.5	**50**
Antenna Size (λ^3)	6.72×10^{-5}	23.94×10^{-5}	27.6×10^{-5}	0.0256×10^{-5}	7.056×10^{-5}	$\mathbf{8.7 \times 10^{-5}}$
System Type	Capsule	Capsule	Capsule/Implantable	Capsule	Implantable	**Capsule**
Antenna Position	Inside	Inside	Inside	Inside	Inside	**Dome**
Transparency	No	No	No	No	No	**Yes**

where d is the distance between transmitter and receiver, γ represents the path-loss exponent, and S_e characterizes the shadowing effect, which describes the impact of obstacles on transmission. As illustrated in Fig. 5.16, effective wireless communication links are tested for distances of 20 m, 15 m, 10 m, and 7 m at data rates of 1 Mbps, 10 Mbps, 25 Mbps, and 78 Mbps, respectively, with more than 20 dB margin. This threshold is selected to ensure a more reliable and stable wireless link [25]. Furthermore, considering the high data rate demands of indoor bio-telemetry applications, a range of 5 - 10 meters may be of particular interest [27]. Table 5.2 compares the proposed antenna with previously reported designs. The proposed model achieves the widest fractional bandwidth of 50% while maintaining a compact electrical size of 8.7×10^{-5} λ^3 at 2.45 GHz. Unlike conventional antennas mounted inside the capsule, this design adopts a transparent dome configuration, providing both optical transparency and stable electromagnetic performance. This demonstrates its advantage in achieving compact, wideband, and visually compatible integration for WCE applications.

5.5 Conclusion

This study established a comprehensive mapping model between optical transparency and electrical conductivity, covering the full workflow from design and optimization to fabrication and experimental characterization. The relationship between transparency, ranging from 50% to 90%, and effective conductivity was systematically characterized over the 0–6 GHz frequency band, providing quantitative guidance for transparent antenna design under radio-frequency excitation.

Based on the developed mapping model, a transparent circular patch antenna employing a coplanar waveguide (CPW) feed was designed using a material configuration corresponding to 70% optical transparency. The proposed antenna features a compact geometry with a diameter of 10 mm and a thickness of 2 mm, enabling direct integration on the dome of a wireless capsule endoscope. This placement strategy effectively utilizes the previously underexploited dome region while preserving the optical functionality required for the embedded imaging module.

Experimental results indicate that the fabricated antenna operates over the 2.1–3.5 GHz frequency range, achieving a fractional bandwidth of approximately 50%, which satisfies ultra-wideband performance requirements. A measured peak gain of –4.6 dBi was obtained, and the calculated specific absorption rate (SAR) values remained well below the IEEE safety limits, confirming compliance with biomedical exposure standards. Furthermore, radiation pattern analysis demonstrates robust link redundancy, which is particularly advantageous for maintaining reliable biotelemetry communication under the dynamic orientation and heterogeneous tissue environment encountered in WCE applications.

Overall, this work establishes a practical and scalable foundation for the design of transparent antennas and, for the first time, demonstrates the feasibility of integrating optical and electromagnetic functionalities within the confined volume of a wireless capsule endoscope. The methodologies and insights presented in this chapter complement the conformal and miniaturized antenna solutions discussed in the preceding chapters, and collectively contribute to a unified antenna design framework for space-efficient, high-capacity, and application-aware implantable medical systems. These contributions are summarized and further discussed in the final chapter, together with potential directions for future research.

CHAPTER 6

General Conclusion and Future Work

6.1 Thesis Summary

This thesis investigated antenna design methodologies for wireless capsule endoscopy (WCE) under stringent constraints on size, bandwidth, integration, and in-body electromagnetic environments. Starting from the relationship between resonance and bandwidth, a staged antenna design framework was established to address space efficiency, detuning robustness, and high-capacity wireless telemetry in WCE systems.

The research was structured in three progressive stages. First, a flexible conformal ultra-wideband (UWB) antenna was proposed to utilise the capsule inner wall while maintaining stable impedance behaviour under bending and tissue loading. Second, a miniaturised dual-element multiple-input multiple-output (MIMO) antenna system was developed using dielectric hollowing and compact conformal layouts to enhance link robustness and channel capacity within a capsule-compatible volume. Third, transparent antenna technology was introduced to enable radiating elements to share the camera-facing region without compromising optical functionality. Through full-wave simulations, fabrication, and experimental validation in tissue-equivalent environments, the proposed designs demonstrated practical feasibility for WCE telemetry and compliance with SAR-related safety considerations.

6.2 Key Contributions

The main contributions of this thesis can be summarised as follows:

- A multi-resonance-based design rationale was established to explain the transition from narrowband operation to UWB behaviour, providing a unified perspective for compact biomedical antenna design.
- A flexible conformal UWB antenna was developed for WCE, enabling wide impedance bandwidth while conforming to the capsule inner cylindrical wall.
- A highly miniaturised conformal MIMO antenna system was proposed using dielectric hollowing, achieving wideband operation with low correlation and improved spatial diversity within a small volume suitable for capsule integration.
- A transparency–conductivity mapping model was experimentally developed for inkjet-printed silver mesh structures over a wide frequency range, enabling quantitative transparent antenna design.
- Transparent antenna technology was demonstrated for WCE camera-region integration, supporting optical transparency while maintaining RF functionality.

6.3 Limitations and Practical Considerations

Despite the promising results, several limitations remain and suggest clear directions for further investigation. First, the electromagnetic evaluation relied on homogeneous or simplified tissue-equivalent models and ex-vivo measurements, which cannot fully represent organ-level heterogeneity, peristaltic motion, and dynamic capsule orientation encountered in vivo. Second, while wideband impedance matching was achieved, realised in-body radiation efficiency and link robustness can still be sensitive to local tissue composition and proximity to other capsule components (battery, camera module, LEDs, and housing), which were not fully co-modelled as a complete commercial capsule assembly. Third, for the transparent mesh conductors, a fundamental trade-off exists between optical transparency and RF loss, and long-term stability (e.g., conductivity drift due to oxidation, humidity, or mechanical micro-cracking) was not systematically characterised. Finally, the current prototypes focused on antenna-level validation; end-to-end system integration aspects such as transceiver constraints, impedance transformation within the packaged capsule, and repeatable manufacturing tolerances require additional engineering effort.

6.4 Future Work Directions

To extend this thesis toward next-generation WCE platforms, future work is outlined as several research themes that could each constitute substantial doctoral-level projects.

6.4.1 Capsule-level co-design

A critical next step is to perform joint optimisation of the antenna(s), capsule housing, and internal electronics (battery, camera module, LEDs, interconnects, and shielding). Such co-design should account for near-field coupling and detuning caused by neighbouring components and should quantify system-level metrics (realised gain/efficiency in tissue, link margin under orientation changes, and SAR). Methodologically, this theme would combine full-wave simulation with detailed CAD packaging, followed by repeatable prototype integration and measurement in anatomically representative phantoms. The outcome would be a validated design workflow that bridges antenna prototypes and manufacturable capsule assemblies.

6.4.2 In-body MIMO and channel study

While MIMO shows strong potential for improving capacity and reliability, practical deployment requires a channel-aware framework that links antenna metrics (isolation, ECC, and pattern diversity) to achievable throughput under realistic in-body fading. This theme would involve: (i) developing capsule-specific in-body channel models across GI segments; (ii) experimentally extracting MIMO channel matrices using heterogeneous phantoms and different capsule orientations; and (iii) quantifying capacity/outage performance under bandwidth and power constraints. Antenna designs could further explore diversity-driven architectures (pattern/polarisation diversity) and compact decoupling strategies that remain feasible inside capsule-scale volumes.

6.4.3 Transparent antennas and reliability

Transparent antennas open a route to utilise the camera-facing region; however, future systems would benefit from multifunctional structures that combine transparency with MIMO, circular polarisation robustness, and potentially sensing/energy functions. Key research questions include: how to maintain stable conductivity and adhesion over time, how to design mesh geometries that minimise RF loss while meeting optical requirements, and how encapsulation influences both optical and RF performance. A systematic study could include accelerated aging (humidity/temperature, bending cycles), conductivity drift modelling, and sensitivity analysis to predict long-term efficiency degradation. The outcome would be design rules for lifetime-aware transparent antennas suitable for biomedical device integration.

Bibliography

[1] G. Iddan, G. Meron, A. Glukhovsky, and P. Swain, “Wireless capsule endoscopy,” *Nature*, vol. 405, no. 6785, pp. 417–417, 2000. (document), 1.1, 1.1.2

[2] S. H. Lee, J. Lee, Y. J. Yoon, S. Park, C. Cheon, K. Kim, and S. Nam, “A wideband spiral antenna for ingestible capsule endoscope systems: Experimental results in a human phantom and a pig,” *IEEE Transactions on Biomedical Engineering*, vol. 58, no. 6, pp. 1734–1741, 2011. (document), 2.1, 2.1.1

[3] C. Liu, Y.-X. Guo, and S. Xiao, “Circularly polarized helical antenna for ism-band ingestible capsule endoscope systems,” *IEEE Transactions on Antennas and Propagation*, vol. 62, no. 12, pp. 6027–6039, 2014. (document), 2.2, 2.1.1

[4] J. Wang, M. Leach, E. G. Lim, Z. Wang, R. Pei, and Y. Huang, “An implantable and conformal antenna for wireless capsule endoscopy,” *IEEE Antennas and Wireless Propagation Letters*, vol. 17, no. 7, pp. 1153–1157, 2018. (document), 2.3, 2.1.1, 4.2

[5] R. Li and Y. Guo, “A conformal uwb dual-polarized antenna for wireless capsule endoscope systems,” *IEEE Antennas and Wireless Propagation Letters*, vol. 20, no. 4, pp. 483–487, 2021. (document), 2.4, 2.1.2

[6] H. Alwafi and A. Alsharif, “Trends in hospital admissions and prescribing due to diseases of the digestive system in england and wales between 1999 and 2019: An ecological study,” *Medicine*, vol. 103, no. 15, p. e37673, 2024. 1.1.1

[7] A. J. Alazemi and A. Iqbal, “A compact and wideband mimo antenna for high-data-rate biomedical ingestible capsules,” *Scientific Reports*, vol. 12, no. 1, p. 14290, 2022. 2.1, 4.2

[8] R. Das and H. Yoo, “A wideband circularly polarized conformal endoscopic antenna system for high-speed data transfer,” *IEEE Transactions on Antennas and Propagation*, vol. 65, no. 6, pp. 2816–2826, 2017. 2.1, 4.2

[9] K. Zhang, C. Liu, X. Liu, H. Cao, Y. Zhang, X. Yang, and H. Guo, “A conformal differentially fed antenna for ingestible capsule system,” *IEEE Transactions on Antennas and Propagation*, vol. 66, no. 4, pp. 1695–1703, 2018. 2.1

[10] K. Liu, R. Liu, W. Cui, K. Zhang, M. Wang, C. Fan, H. Zheng, and E. Li, “Design of conformal spiral dual-band antenna for wireless capsule system,” *IEEE Access*, vol. 9, pp. 117 349–117 357, 2021. 2.1, 3.1.2, 4.2

[11] Z. Duan, H. Xu, S. S. Gao, and W. Geyi, “A circularly polarized omnidirectional antenna for wireless capsule endoscope system,” *IEEE Transactions on Antennas and Propagation*, vol. 69, no. 4, pp. 1896–1907, 2021. 2.1, 3.1.2

[12] W. Lei and Y.-X. Guo, “Design of a dual-polarized wideband conformal loop antenna for capsule endoscopy systems,” *IEEE Transactions on Antennas and Propagation*, vol. 66, no. 11, pp. 5706–5715, 2018. 2.1, 3.1.2, 4.2

[13] K. N. Ketavath, D. Gopi, and S. Sandhya Rani, “In-vitro test of miniaturized cpw-fed implantable conformal patch antenna at ism band for biomedical applications,” *IEEE Access*, vol. 7, pp. 43 547–43 554, 2019. 2.1

[14] P. M. Izdebski, H. Rajagopalan, and Y. Rahmat-Samii, “Conformal ingestible capsule antenna: A novel chandelier meandered design,” *IEEE Transactions on Antennas and Propagation*, vol. 57, no. 4, pp. 900–909, 2009. 2.2.4

[15] K. Zhang, C. Liu, X. Liu, H. Cao, Y. Zhang, X. Yang, and H. Guo, “A conformal differentially fed antenna for ingestible capsule system,” *IEEE Transactions on Antennas and Propagation*, vol. 66, no. 4, pp. 1695–1703, 2018. 2.2.4, 3.1.2, 4.2

[16] Z. Bao, Y.-X. Guo, and R. Mittra, “Conformal capsule antenna with reconfigurable radiation pattern for robust communications,” *IEEE Transactions on Antennas and Propagation*, vol. 66, no. 7, pp. 3354–3365, 2018. 2.2.4

[17] J. Wang, M. Leach, E. G. Lim, Z. Wang, R. Pei, and Y. Huang, “An implantable and conformal antenna for wireless capsule endoscopy,” *IEEE Antennas and Wireless Propagation Letters*, vol. 17, no. 7, pp. 1153–1157, 2018. 3.1.1

[18] D. Nikolayev, M. Zhadobov, L. Le Coq, P. Karban, and R. Sauleau, “Robust ultraminiature capsule antenna for ingestible and implantable applications,” *IEEE Transactions on Antennas and Propagation*, vol. 65, no. 11, pp. 6107–6119, 2017. 3.1.1

[19] M. Suzan Miah, A. N. Khan, C. Icheln, K. Haneda, and K.-I. Takizawa, “Antenna system design for improved wireless capsule endoscope links at 433 mhz,” *IEEE Transactions on Antennas and Propagation*, vol. 67, no. 4, pp. 2687–2699, 2019. 3.1.1, 4.2

[20] R. Li and Y. Guo, “A conformal uwb dual-polarized antenna for wireless capsule endoscope systems,” *IEEE Antennas and Wireless Propagation Letters*, vol. 20, no. 4, pp. 483–487, 2021. 3.1.1, 5.1

[21] A. Basir, M. Zada, Y. Cho, and H. Yoo, “A dual-circular-polarized endoscopic antenna with wideband characteristics and wireless biotelemetric link characterization,” *IEEE Transactions on Antennas and Propagation*, vol. 68, no. 10, pp. 6953–6963, 2020. 3.1.2

[22] C. Gabriel, S. Gabriel, and Y. Corthout, “The dielectric properties of biological tissues: I. literature survey,” *Physics in medicine & biology*, vol. 41, no. 11, p. 2231, 1996. 3.1.3, 4.3.1, 5.3.1

[23] R. Das and H. Yoo, “A wideband circularly polarized conformal endoscopic antenna system for high-speed data transfer,” *IEEE Transactions on Antennas and Propagation*, vol. 65, no. 6, pp. 2816–2826, 2017. 3.2, 3.4

[24] Z. Duan, H. Xu, S. S. Gao, and W. Geyi, “A circularly polarized omnidirectional antenna for wireless capsule endoscope system,” *IEEE Transactions on Antennas and Propagation*, vol. 69, no. 4, pp. 1896–1907, 2020. 3.2

[25] N. R. Challa and R. S, “Design of multiband implantable loop antenna for in body applications,” in *2015 Conference on Power, Control, Communication and Computational Technologies for Sustainable Growth (PCCCTSG)*, 2015, pp. 239–242. 3.2, 4.4.3, 4.2, 5.4.3, 5.4.4

[26] A. Basir, M. Zada, Y. Cho, and H. Yoo, “A dual-circular-polarized endoscopic antenna with wideband characteristics and wireless biotelemetric link characterization,” *IEEE Transactions on Antennas and Propagation*, vol. 68, no. 10, pp. 6953–6963, 2020. 3.2, 3.4, 4.4.4, 5.4.4

[27] Z. Bao, Y.-X. Guo, and R. Mittra, “Single-layer dual-/tri-band inverted-f antennas for conformal capsule type of applications,” *IEEE Transactions on Antennas and Propagation*, vol. 65, no. 12, pp. 7257–7265, 2017. 3.2, 5.4.4

[28] G. Zhang, X. Song, Z. Yu, and X. An, “A symmetrical closed-loop conformal antenna with wideband for capsule endoscope,” *IEEE Antennas and Wireless Propagation Letters*, vol. 20, no. 10, pp. 1918–1922, 2021. 3.2, 4.4.5

[29] S. Hayat, S. A. A. Shah, and H. Yoo, “Miniaturized dual-band circularly polarized implantable antenna for capsule endoscopic system,” *IEEE Transactions on Antennas and Propagation*, vol. 69, no. 4, pp. 1885–1895, 2021. 3.3, 4.2, 5.2

[30] Y. Wang, B. Huang, and S. Yan, “A conformal four-antenna module for capsule endoscope mimo operation,” *IEEE Transactions on Antennas and Propagation*, vol. 70, no. 11, pp. 10 270–10 285, 2022. 4.2, 4.2

[31] J. Shang and Y. Yu, “An ultrawideband capsule antenna for biomedical applications,” *IEEE Antennas and Wireless Propagation Letters*, vol. 18, no. 12, pp. 2548–2551, 2019. 4.2

[32] ——, “An ultrawideband and conformal antenna for wireless capsule endoscopy,” *Microwave and Optical Technology Letters*, vol. 62, no. 2, pp. 860–865, 2020. 4.2

[33] Y. A. Salchak, N. M. Albadri, M. T. Worsey, H. G. Espinosa, and D. V. Thiel, "Surface electric field variations due to different human postures for wireless endoscopy applications," *IEEE Transactions on Instrumentation and Measurement*, vol. 70, pp. 1–11, 2021. 4.2

[34] H. Q. Ngo, E. G. Larsson, and T. L. Marzetta, "Energy and spectral efficiency of very large multiuser mimo systems," *IEEE Transactions on Communications*, vol. 61, no. 4, pp. 1436–1449, 2013. 4.2

[35] A. J. Alazemi and A. Iqbal, "A high data rate implantable mimo antenna for deep implanted biomedical devices," *IEEE Transactions on Antennas and Propagation*, vol. 70, no. 2, pp. 998–1007, 2022. 4.2, 4.4.4, 5.2

[36] A. Iqbal, M. Al-Hasan, I. B. Mabrouk, and M. Nedil, "A compact implantable mimo antenna for high-data-rate biotelemetry applications," *IEEE Transactions on Antennas and Propagation*, vol. 70, no. 1, pp. 631–640, 2022. 4.2, 5.2

[37] S. Xiao, C. Liu, Y. Li, X. M. Yang, and X. Liu, "Small-size dual-antenna implantable system for biotelemetry devices," *IEEE Antennas and Wireless Propagation Letters*, vol. 15, pp. 1723–1726, 2016. 4.2, 4.4.3, 5.4.3

[38] A. Iqbal, M. Al-Hasan, I. B. Mabrouk, and M. Nedil, "Scalp-implantable mimo antenna for high-data-rate head implants," *IEEE Antennas and Wireless Propagation Letters*, vol. 20, no. 12, pp. 2529–2533, 2021. 4.2, 5.1

[39] K. Liu, Z. Li, W. Cui, K. Zhang, M. Wang, C. Fan, H. Zheng, and E. Li, "Investigation of conformal mimo antenna for implantable devices based on theory of characteristic modes," *IEEE Transactions on Antennas and Propagation*, vol. 70, no. 12, pp. 11 324–11 334, 2022. 4.2

[40] Y. Wang, B. Huang, and S. Yan, "A conformal four-antenna module for capsule endoscope mimo operation," *IEEE Transactions on Antennas and Propagation*, vol. 70, no. 11, pp. 10 270–10 285, 2022. 4.2

[41] G. Gauthier, A. Courtay, and G. Rebeiz, "Microstrip antennas on synthesized low dielectric-constant substrates," *IEEE Transactions on Antennas and Propagation*, vol. 45, no. 8, pp. 1310–1314, 1997. 4.3

[42] C. Xiao, S. Hao, and Y. Zhang, "915 mhz miniaturized loop conformal antenna for capsule endoscope," *IEEE Transactions on Antennas and Propagation*, vol. 70, no. 11, pp. 10 233–10 244, 2022. 4.3.2

[43] G. Gauthier, A. Courtay, and G. Rebeiz, "Microstrip antennas on synthesized low dielectric-constant substrates," *IEEE Transactions on Antennas and Propagation*, vol. 45, no. 8, pp. 1310–1314, 1997. 4.3.3

[44] I. Gani and H. Yoo, "Multi-band antenna system for skin implant," *IEEE Microwave and Wireless Components Letters*, vol. 26, no. 4, pp. 294–296, 2016. 4.4.4

[45] A. Iqbal, M. Al-Hasan, I. B. Mabrouk, and T. A. Denidni, "Capsule endoscopic mimo antenna with radiation pattern and polarization diversity," *IEEE Transactions on Antennas and Propagation*, vol. 71, no. 4, pp. 3146–3154, 2023. 5.1, 5.2

[46] L. Chang, A. Iqbal, A. Basir, R. B. Simorangkir, and I. B. Mabrouk, "Conformal mimo ultra-wideband antenna design for high-speed wireless telemetry in capsule endoscopy systems," *IEEE Transactions on Antennas and Propagation*, 2024. 5.1

[47] F. Colombel, X. Castel, M. Himdi, G. Legeay, S. Vigneron, and E. Motta Cruz, "Ultrathin metal layer, ito film and ito/cu/ito multilayer towards transparent antenna," *IET science, measurement & technology*, vol. 3, no. 3, pp. 229–234, 2009. 5.1

[48] S. Sheikh, M. Shokooh-Saremi, and M.-M. Bagheri-Mohagheghi, "Transparent microstrip patch antenna based on fluorine-doped tin oxide deposited by spray pyrolysis technique," *IET Microwaves, Antennas & Propagation*, vol. 9, no. 11, pp. 1221–1229, 2015. 5.1

[49] S. H. Kang and C. W. Jung, "Transparent patch antenna using metal mesh," *IEEE Transactions on Antennas and Propagation*, vol. 66, no. 4, pp. 2095–2100, 2018. 5.1

[50] Y. Yao, Y. Shao, J. Zhang, and J. Zhang, "A transparent antenna using metal mesh for uwb mimo applications," *IEEE Transactions on Antennas and Propagation*, vol. 71, no. 5, pp. 3836–3844, 2023. 5.1

[51] D. Lim and S. Lim, "Optically transparent and rollable metafilm for electromagnetic absorption using screen printed metal mesh," *IEEE Antennas and Wireless Propagation Letters*, vol. 24, no. 3, pp. 686–690, 2025. 5.1

[52] M. A. Shah, D.-G. Lee, B.-Y. Lee, and S. Hur, "Classifications and applications of inkjet printing technology: A review," *IEEE Access*, vol. 9, pp. 140 079–140 102, 2021. 5.1

[53] F. Hermerschmidt, S. A. Choulis, and E. J. List-Kratochvil, "Implementing inkjet-printed transparent conductive electrodes in solution-processed organic electronics," *Advanced Materials Technologies*, vol. 4, no. 5, p. 1800474, 2019. 5.1

[54] M. S. Singh, J. Ghosh, S. Ghosh, and A. Sarkhel, "Miniaturized dual-antenna system for implantable biotelemetry application," *IEEE Antennas and Wireless Propagation Letters*, vol. 20, no. 8, pp. 1394–1398, 2021. 5.2